Development of a synthetic phase contrast imaging diagnostic for turbulence studies at Wendelstein 7-X

S K Hansen[1], M Porkolab[1], J-P Bähner[1], Z Huang[1], A von Stechow[2], O Grulke[2,3], E M Edlund[4], F Wilms[5], A Bañón Navarro[5], F Jenko[5] and E Sánchez[6]

[1] Plasma Science and Fusion Center, Massachusetts Institute of Technology, Cambridge, MA 02139, USA

[2] Max-Planck-Institut für Plasmaphysik, D-17491 Greifswald, Germany

[3] Department of Physics, Technical University of Denmark, DK-2800 Kgs. Lyngby, Denmark

[4] State University of New York College at Cortland, Cortland, NY 13045, USA

[5] Max-Planck-Institut für Plasmaphysik, D-85748 Garching, Germany

[6] Laboratorio Nacional de Fusión, CIEMAT, E-28040 Madrid, Spain

E-mail: `soerenkh@psfc.mit.edu`

Abstract. We present a synthetic phase contrast imaging (PCI) diagnostic for studying turbulence at the Wendelstein 7-X (W7-X) stellarator. We first describe the implemented instrument response model, which captures diffraction effects, detector noise, and the long-wavelength cutoff due to the phase plate of the PCI system. To verify the instrument response model, we show that it is capable of reproducing the PCI signal generated by the sound wave speaker used for calibration at W7-X. Next, we discuss calculation of synthetic PCI signals based on the global, nonlinear gyrokinetic codes GENE-3D and EUTERPE, including results from some of the first stellarator simulations of this type with kinetic electrons in GENE-3D. While the simulations used in this work lack a neoclassical radial electric field, which is crucial for reproducing experimental PCI signals, they do indicate that the dominant rotation direction and velocities of the turbulent fluctuations can be inferred from the wave number-frequency spectra of the PCI signals, as expected. The synthetic PCI wave number spectra are further shown to be similar to those of the line-integrated fluctuating electron density, with distinct differences between adiabatic and kinetic electron simulations, explainable by previously published turbulence models. For example, the wave number spectra of all adiabatic electron simulations analyzed here follow a power law with an exponent close to -5 for sufficiently large wave numbers. This indicates that universal features of electron density turbulence at W7-X may be studied using the PCI system.

Keywords: PCI, synthetic diagnostics, plasma turbulence, kinetic electrons, GENE-3D, EUTERPE, Wendelstein 7-X

1. Introduction

The quest to realize magnetic confinement fusion as a viable energy source has been hampered by the existence of significantly higher transport levels than those expected based on simple classical collisional estimates. While the proper inclusion of geometric effects on collisional transport, known as neoclassical transport, does lead to transport levels closer to the ones observed experimentally, an additional contribution, known as anomalous transport, remains in most cases and is often found to dominate the overall transport level. Anomalous transport is attributed to turbulence generated by microinstabilities driven by the temperature and density gradients in the plasma. In the electrostatic limit, the microinstabilities may be split into ion temperature gradient (ITG) modes, trapped electron modes (TEMs), and electron temperature gradient (ETG) modes [1], according to the main source of free energy that drives them.

Wendelstein 7-X (W7-X) is the largest stellarator optimized for reduced neoclassical losses, which causes anomalous transport to play a dominant role in most scenarios [2, 3]. Considering the reversed (negative) shear and the near maximum-J, high-mirror configuration when operating at high β-values (kinetic plasma pressure divided by magnetic pressure) [1], W7-X can investigate a significant number of important topics relevant to understanding plasma turbulence and related transport both in stellarators and tokamaks. These include suppression of ETG turbulent transport in stellarators and reversed shear tokamaks [4], suppression of classical TEM turbulence in maximum-J stellarators [1, 5], the stability valley between ITG and TEM dominated regimes [6], suppression of turbulence during pellet [7] and boron [8] injection, suppression of turbulence by fast ions [9], and improved confinement with neutral beam heating [10].

In order to investigate plasma turbulence experimentally, a number of dedicated plasma diagnostics have been devolped, including probe measurements [11], Doppler reflectometry [12–15], electromagnetic wave scattering [16], and phase contrast imaging (PCI) [17–25]. At W7-X, probe measurements are used to characterize scrape-off layer and edge turbulence [11], while Doppler reflectometry provides localized measurements of turbulence in the edge and outer core regions [15], and finally PCI provides line-integrated measurements of core turbulence [21, 24, 25].

The PCI method, which is the main subject of the present paper, was developed by Zernike [26] and first applied to high-density, low-temperature plasmas by Presby and Finkelstein [27]. The first application to fusion plasmas was made by Weisen at the TCA tokamak [17]. PCI systems have since been installed at the DIII-D [18, 22, 23, 28–30], Alcator C-Mod [29, 31–38], TCV [19, 39, 40], and HL-2A [41] tokamaks, as well as the LHD [42, 43] and W7-X [21, 24, 25, 44] stellarators.

In its most basic fusion-relevant form, PCI provides measurements of the fluctuating phase shift of a laser beam induced by a plasma, which may be mapped to the line-integrated fluctuating electron density of the plasma [20, 25, 29, 32–38, 40]. Although the line-integrated nature of PCI measurements means that information can in principle be obtained from the entire laser line-of-sight (LoS), it also makes pin-pointing the origin

of the PCI signal difficult. It is possible to localize PCI measurements to some extent through the use of rotating masks [24, 29, 30], although this requires knowledge of the magnetic geometry and involves a non-trivial instrument response [29,30]. Additionally, PCI cuts off long wavelength fluctuations, owing to the necessity of separating the unscattered and small-angle scattered parts of the laser beam to image the fluctuating phase shift [17, 28, 29]. Thus, in order to interpret PCI measurements without having to make a number of assumptions whose validity is difficult assess, it is very useful to implement a synthetic PCI diagnostic, enabling computation of the PCI signal expected for a given fluctuating electron density profile. Synthetic PCI diagnostics have already been used to study turbulence [20,33,40], Alfvén eigenmodes [34–37], and mode conversion of ion cyclotron waves [29, 32, 38] at the DIII-D, Alcator C-Mod, and TCV tokamaks. Additionally, some early results from synthetic PCI studies of turbulence at W7-X have been presented in [25, 45]. We also note that synthetic diagnostics are crucial to correctly interpret data from other plasma diagnostics, particularly Doppler reflectometry [12–14], and for validation of plasma turbulence models [46]. This paper provides a detailed description of the synthetic PCI diagnostic developed for turbulence studies at W7-X and presents the first synthetic PCI investigation of stellarator turbulence including a kinetic electron response.

Due to the line-integrated nature of PCI measurements, the turbulence models utilized for synthetic PCI diagnostics must be able to compute the fluctuating electron density in the majority of the radial, toroidal, and poloidal regions covered by the PCI LoSs. The central PCI LoSs utilized at W7-X [21, 24, 25] thus demand global simulations. Additionally, experimental PCI signals generally originate from fully developed turbulence, meaning that the simulations must be nonlinear as well. To construct an accurate synthetic PCI diagnostic for core turbulence, we therefore require global, nonlinear gyrokinetic turbulence simulations of the W7-X geometry. Such simulations are computationally demanding and have only recently become available. Here, we focus on runs performed using the GENE-3D [47–50] and EUTERPE [51] codes, while noting that efforts to include runs from the GTC code [52,53] are ongoing. Most global, nonlinear gyrokinetic simulations of stellarator geometries performed to date have assumed an adiabatic electron response, meaning that they only capture ITG turbulence [1]. While such turbulence is indeed found to be dominant in usual electron cyclotron resonance heated (ECRH) W7-X plasmas [25], studies of predictions such as the stability valley between ITG and TEM dominated regimes [6], the suppression of classical TEM turbulence in maximum-J configurations [1, 5], and the suppression of ETG turbulent transport [4] require the inclusion of a kinetic electron response. Some early simulations including a kinetic electron response performed with the GENE-3D code are discussed here, although we note that their limited spatial resolution only enables modifications of ITG turbulence to be studied. We further note that the simulations analyzed in this work do not include a neoclassical radial electric field, which is the main factor determining the plasma rotational velocity observed by the PCI system at W7-X [25]. The synthetic PCI investigations presented here are therefore

mainly focused on describing the integration of the simulations into the synthetic PCI diagnostic and on identifying universal features of the simulations in the spectral ranges covered by the PCI system at W7-X to facilitate future synthetic and experimental PCI investigations.

The remainder of this paper is organized as follows. Section 2 describes the PCI instrument response model of the W7-X synthetic PCI diagnostic, including considerations of detector noise, the numerical scheme used, and some results verifying that the PCI sound wave calibration signal [24,54] can be reproduced. Section 3 discusses the inclusion of gyrokinetic simulation output from the GENE-3D and EUTERPE codes in the synthetic PCI diagnostic, focusing on the schemes used for obtaining the line-integrated fluctuating electron density profiles and on the features of the computed power spectra (wave number-frequency and wave number). Finally, in Section 4, conclusions are drawn.

2. Instrument response model

In order to implement a synthetic diagnostic, a foward model providing the response of the PCI system for particular plasma conditions is necessary. Here, we follow an approach similar to that of [17, 28]. A schematic of the W7-X PCI system, including only the elements relevant for computing the response of the synthetic diagnostic, is shown in figure 1. We denote the coordinate parallel to the optical axis by z and the coordinates perpendicular to the optical axis by $\mathbf{x}_\perp = (x, y)$, where the x-direction is the measurement direction of the 1D PCI detector arrays at W7-X [21,24]. As seen in figure 1, we consider a monochromatic, collimated laser beam, with free-space wavelength λ_0 and electric field profile $\mathbf{E}_0(\mathbf{x}_\perp)$, incident on the plasma. For the CO_2 laser used at W7-X [21, 24], $\lambda_0 = 10.6\,\mu$m and $\mathbf{E}_0$ is taken to be Gaussian, i.e.,

$$\mathbf{E}_0(\mathbf{x}_\perp) = \mathbf{e}_0 \sqrt{\frac{4\eta_0 P_0}{\pi W_0^2}}\, \mathrm{e}^{-(x^2+y^2)/W_0^2}, \tag{1}$$

where $\mathbf{e}_0$ is the polarization unit vector, η_0 is the impedance of vacuum, P_0 is the effective laser power accounting for reductions due to beam splitters through the optical system [24] (typically 6.3 W during the previous operation phases of W7-X; the phase plate is considered separately), and W_0 is the 1/e electric field radius of the Gaussian beam. In the Raman−Nath limit [55], which is relevant for PCI measurements [28], the effect of the plasma on the laser beam is determined by the phase shift, ϕ, induced along each LoS. Thus, the electric field profile after the beam has passed through the plasma may be expressed as

$$\mathbf{E}_{\mathrm{obj}}(\mathbf{x}_\perp) = \mathbf{E}_0(\mathbf{x}_\perp)\, \mathrm{e}^{\mathrm{i}\phi(\mathbf{x}_\perp)}. \tag{2}$$

Since the PCI laser frequency (28.3 THz at W7-X) is far above the electron plasma and cyclotron frequencies ($\lesssim 100\,$GHz at W7-X), the response of the plasma to the laser

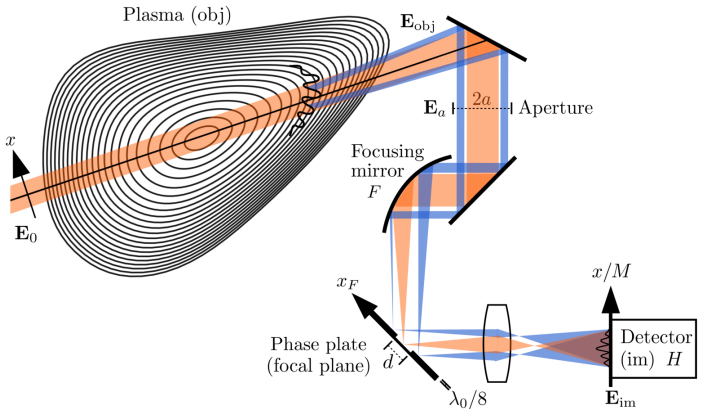

Figure 1. Schematic drawing of the elements implemented in the synthetic PCI diagnostic for W7-X. The symbols are described in the main text.

may be considered essentially unmagnetized, leading to a refractive index [56]

$$N(\mathbf{x}_\perp, z) = \sqrt{1 - \frac{r_e \lambda_0^2}{\pi} n_e(\mathbf{x}_\perp, z)} \approx 1 - \frac{r_e \lambda_0^2}{2\pi} n_e(\mathbf{x}_\perp, z), \tag{3}$$

where n_e is the electron number density, r_e is the classical electron radius, and the last approximation is valid for $n_e \ll \pi/(r_e\lambda_0^2) = 9.92 \times 10^{24}\,\mathrm{m}^{-3}$, which is always satisfied at W7-X [3]. Using (3), ϕ may be expressed as

$$\phi(\mathbf{x}_\perp) = \frac{2\pi}{\lambda_0} \int_{\rm LoS} N(\mathbf{x}_\perp, z)\,\mathrm{d}z \approx \frac{2\pi}{\lambda_0} L - r_e \lambda_0 \int_{\rm LoS} n_e(\mathbf{x}_\perp, z)\,\mathrm{d}z, \tag{4}$$

with L being the length of the LoS. Further, we may write $\phi = \phi_0 + \tilde{\phi}$, where ϕ_0 is a mean background phase shift and $\tilde{\phi} = -r_e\lambda_0 \int_{\rm LoS} \tilde{n}_e\,\mathrm{d}z$ is a fluctuating phase shift, which contains the line-integrated information concerning the fluctuating electron density, $\tilde{n}_e$, of interest to PCI. The spatio-temporal variation of ϕ_0 may be neglected [17, 28]. On the other hand, it can be assumed that $|\tilde{\phi}| \ll 1$ when $|\int_{\rm LoS} \tilde{n}_e\,\mathrm{d}z| \ll 1/(r_e\lambda_0) = 3.35 \times 10^{19}\,\mathrm{m}^{-2}$, which is generally true for the PCI system at W7-X [21, 24]. With the above separation and approximations, we obtain,

$$\mathbf{E}_{\rm obj}(\mathbf{x}_\perp) \approx \mathbf{E}_0(\mathbf{x}_\perp)\,\mathrm{e}^{\mathrm{i}\phi_0}\,\mathrm{e}^{\mathrm{i}\tilde{\phi}(\mathbf{x}_\perp)} \approx \mathbf{E}_0(\mathbf{x}_\perp)\,\mathrm{e}^{\mathrm{i}\phi_0}[1 + \mathrm{i}\tilde{\phi}(\mathbf{x}_\perp)]. \tag{5}$$

It is evident from (2) and (5) that the plasma only modulates the phase of the laser beam, while it leaves the intensity, $I = |\mathbf{E}|^2/(2\eta_0)$, unchanged. Since I is the quantity that is ultimately observable by the detector array, the PCI system must convert the phase shift in the object plane into an intensity variation in the image plane. The bracket in the last approximation of (5) shows that the beam in the object plane consists of an unscattered part, characterized by the 1, and a (small-angle) scattered part, characterized by the $\mathrm{i}\tilde{\phi}$, within the Born approximation [28]. The phase modulation may be converted into an intensity modulation if the phase of the unscattered part of the beam can be shifted by $\pm\pi/2$, as this will convert the 1 into $\pm\mathrm{i}$, leading to $I \approx |\mathbf{E}_0|^2(1 \pm 2\tilde{\phi})/(2\eta_0)$. Such a selective phase shift may be achieved by placing a phase plate, which is a mirror with a central groove of depth $\lambda_0/8$, in the focal plane of a focusing mirror, as seen in

figure 1. The unscattered part of the beam will impinge on the groove of the phase plate, while the scattered part will impinge on the main part of the phase plate, and the unscattered part of the beam will thus accumulate an extra phase shift of $\pi/2$ relative to the scattered part.

In order to quantitatively model the effect of the PCI system on the laser beam, we return to the diagram in figure 1. First, the beam passes through a circular aperture of radius a, which causes diffraction that may, to the lowest order, be modeled by modifying $\mathbf{E}_{\mathrm{obj}}$ to

$$\mathbf{E}_a(\mathbf{x}_\perp) = \mathcal{P}_a(\mathbf{x}_\perp)\mathbf{E}_{\mathrm{obj}}(\mathbf{x}_\perp) \approx \mathcal{P}_a(\mathbf{x}_\perp)\mathbf{E}_0(\mathbf{x}_\perp)\,\mathrm{e}^{\mathrm{i}\phi_0}[1+\mathrm{i}\tilde{\phi}(\mathbf{x}_\perp)], \tag{6}$$

where $\mathcal{P}_a$ is a pupil function equal to 1 inside the aperture ($|\mathbf{x}_\perp| < a$) and equal to 0 outside the aperture ($|\mathbf{x}_\perp| > a$) [28]. Next, the beam reflects off the focusing mirror and propagates to the focal plane, where the electric field profile is proportional to the Fourier transform of $\mathbf{E}_a(\mathbf{x}_\perp)$, which we denote $\hat{\mathbf{E}}_a(\mathbf{k}) = \int_{\mathrm{all}\,\mathbf{x}_\perp} \mathbf{E}_a\,\mathrm{e}^{-\mathrm{i}\mathbf{k}\cdot\mathbf{x}_\perp}\,\mathrm{d}\mathbf{x}_\perp$, with $\mathbf{k}$ being a wave vector perpendicular to the beam axis. $\mathbf{k}$ may be mapped to a location in the focal plane, $\mathbf{x}_{F\perp}$, as

$$\mathbf{k} = \frac{2\pi\mathbf{x}_{F\perp}}{\lambda_0 F}, \tag{7}$$

where $F = 2.032\,\mathrm{m}$ (80") [24] is the focal length of the focusing mirror. The phase plate now introduces an extra phase shift of $\pi/2$ to the parts of the beam within its groove, which has a width of $d = 1.1\,\mathrm{mm}$ in the x_F-direction and is additionally covered in a coating with a reflection coefficient $\rho = 0.28$ at W7-X [24], while the parts of the beam outside the groove are simply reflected without any absorption. Thus, after the beam has reflected off the phase plate, its electric field profile is proportional to $\hat{T}\hat{\mathbf{E}}_a$, where $\hat{T}$ is the transfer function of the phase plate, given by

$$\hat{T}(\mathbf{x}_{F\perp}) = 1 - \mathcal{P}_{d/2}(x_F) + \mathrm{i}\sqrt{\rho}\,\mathcal{P}_{d/2}(x_F), \tag{8}$$

with $\mathcal{P}_{d/2}(x_F)$ being a pupil function of the groove, equal to 1 for $|x_F| < d/2$ and equal to 0 for $|x_F| > d/2$. Converting $\hat{T}$ to $\mathbf{k}$ space using (7), yields

$$\hat{T}(\mathbf{k}) = 1 - \mathcal{P}_{k_{\mathrm{min}}}(k_x) + \mathrm{i}\sqrt{\rho}\,\mathcal{P}_{k_{\mathrm{min}}}(k_x), \tag{9}$$

where

$$k_{\mathrm{min}} = \frac{\pi d}{\lambda_0 F} = 1.6\,\mathrm{cm}^{-1} \tag{10}$$

is the minimum value of $|k_x|$ required to not hit the groove at W7-X [24] and acts as a lower bound on the $|k_x|$ of the fluctuations that may be observed by PCI. The laser beam finally proceeds to the detector, which is located at an image plane of the plasma, meaning that the signal will be proportional to the inverse Fourier transform of the signal at the focal plane, $\hat{T}(\mathbf{k})\hat{\mathbf{E}}_a(\mathbf{k})$. The inverse Fourier transform, $\mathbf{g}(\mathbf{x}_\perp) = [1/(2\pi)^2]\int_{\mathrm{all}\,\mathbf{k}} \hat{\mathbf{g}}(\mathbf{k})\,\mathrm{e}^{\mathrm{i}\mathbf{k}\cdot\mathbf{x}_\perp}\,\mathrm{d}\mathbf{k}$, converts a product of Fourier transforms to a convolution of the inverse Fourier transforms, making the electric field amplitude in the image plane, $\mathbf{E}_{\mathrm{im}}$, proportional to

$$(T * \mathbf{E}_a)(\mathbf{x}_\perp) = \int_{\mathrm{all}\,\mathbf{x}'_\perp} T(\mathbf{x}_\perp - \mathbf{x}'_\perp)\mathbf{E}_a(\mathbf{x}'_\perp)\,\mathrm{d}\mathbf{x}'_\perp, \tag{11}$$

where

$$T(\mathbf{x}_\perp) = \delta(\mathbf{x}_\perp) - \hat{\mathcal{P}}_{k_{\min}}(\mathbf{x}_\perp) + \mathrm{i}\sqrt{\rho}\,\hat{\mathcal{P}}_{k_{\min}}(\mathbf{x}_\perp) \tag{12}$$

is the inverse Fourier transform of $\hat{T}(\mathbf{k})$, with δ being the Dirac delta distribution and

$$\hat{\mathcal{P}}_{k_{\min}}(\mathbf{x}_\perp) = \frac{\sin(k_{\min}x)}{\pi x}\delta(y) \tag{13}$$

being the inverse Fourier transform of $\mathcal{P}_{k_{\min}}(\mathbf{k})$. In order to compute the actual $\mathbf{E}_{\mathrm{im}}$, we need to account for the phase shift introduced by propagation of the laser beam through the PCI system, ϕ_{im}, as well as for the magnification of the laser beam, M, created by optics between the phase plate and the image plane [21, 24]. The former effect is accounted for by the inclusion of a phase factor $\mathrm{e}^{\mathrm{i}\phi_{\mathrm{im}}}$, in which we assume that ϕ_{im} is constant across the laser beam, while the latter effect maps $\mathbf{x}_\perp$ in the object plane to $\mathbf{x}_\perp/M$ in the image plane and leads to a multiplication of the electric field amplitude by M to conserve energy [28]. Thus,

$$\mathbf{E}_{\mathrm{im}}\left(\frac{\mathbf{x}_\perp}{M}\right) = M\,\mathrm{e}^{\mathrm{i}\phi_{\mathrm{im}}}(T * \mathbf{E}_a)(\mathbf{x}_\perp). \tag{14}$$

Since the detector elements are sensitive to the power incident on them, P_{det}, we integrate $I_{\mathrm{im}}(\mathbf{x}_\perp/M) = |\mathbf{E}_{\mathrm{im}}(\mathbf{x}_\perp/M)|^2/(2\eta_0) = M^2|(T * \mathbf{E}_a)(\mathbf{x}_\perp)|^2/(2\eta_0)$, over the area of the image plane covered by a detector element,

$$P_{\mathrm{det}} = \int_{\mathrm{det}} I_{\mathrm{im}}\left(\frac{\mathbf{x}_\perp}{M}\right)\mathrm{d}\left(\frac{\mathbf{x}_\perp}{M}\right) = \frac{1}{2\eta_0}\int_{M\times\mathrm{det}} |(T * \mathbf{E}_a)(\mathbf{x}_\perp)|^2\,\mathrm{d}\mathbf{x}_\perp; \tag{15}$$

the last equality converts the integral over the detector element into an integral over the (magnified) image of the detector element in the object plane. The two detector arrays used at W7-X each consist of 32 retangular elements arranged in a line along the x-direction, which roughly corresponds to the poloidal direction in the plasma; each element has a width of $W_{\mathrm{det}} = 0.5\,\mathrm{mm}$ along the x-direction, a height of $h_{\mathrm{det}} = 1\,\mathrm{mm}$ along the y-direction, and the gap between adjacent elements along the x-direction is $W_{\mathrm{gap}} = 50\,\mu\mathrm{m}$ [21, 24]. When analyzing experimental data, a detector element is considered to represent the signal at its center, and by varying $M \in [2.67, 13.33]$ [24], the spacing between the measurement points along the x-axis in the plasma may be varied. This representation gives an upper bound on the $|k_x|$-values that may be resolved by the PCI system at W7-X through the Nyquist wave number of the detector array image,

$$k_{\max} = \frac{\pi}{M(W_{\mathrm{det}} + W_{\mathrm{gap}})} = \frac{57.1\,\mathrm{cm}^{-1}}{M} \leq 21.4\,\mathrm{cm}^{-1}, \tag{16}$$

although we note that phase scintillation due to imperfect alignment between the image plane and the detector array, which is not included in the synthetic PCI model, may lead to a lower value in practice [25].

To obtain an explicit expression for P_{det} from (15), we compute $T * \mathbf{E}_a$ using (6), (11), and (12),

$$\begin{aligned} T * \mathbf{E}_a &= \mathbf{E}_a - \hat{\mathcal{P}}_{k_{\min}} * \mathbf{E}_a + \mathrm{i}\sqrt{\rho}\,\hat{\mathcal{P}}_{k_{\min}} * \mathbf{E}_a \\ &= \mathrm{e}^{\mathrm{i}\phi_0}\left\{\mathcal{P}_a\mathbf{E}_0 - \hat{\mathcal{P}}_{k_{\min}} * (\mathcal{P}_a\mathbf{E}_0) - \sqrt{\rho}\,\hat{\mathcal{P}}_{k_{\min}} * (\mathcal{P}_a\mathbf{E}_0\tilde{\phi})\right. \\ &\qquad \left. + \mathrm{i}\left[\mathcal{P}_a\mathbf{E}_0\tilde{\phi} + \sqrt{\rho}\,\hat{\mathcal{P}}_{k_{\min}} * (\mathcal{P}_a\mathbf{E}_0) - \hat{\mathcal{P}}_{k_{\min}} * (\mathcal{P}_a\mathbf{E}_0\tilde{\phi})\right]\right\}, \end{aligned} \tag{17}$$

and further note that $|T * \mathbf{E}_a|^2$ may be written as

$$|T * \mathbf{E}_a|^2 \approx |\mathcal{P}_a\mathbf{E}_0 - \hat{\mathcal{P}}_{k_{\min}} * (\mathcal{P}_a\mathbf{E}_0)|^2 + \rho\,|\hat{\mathcal{P}}_{k_{\min}} * (\mathcal{P}_a\mathbf{E}_0)|^2 + 2\sqrt{\rho}\,\mathcal{P}_a\mathbf{E}_0^* \cdot \left\{[\hat{\mathcal{P}}_{k_{\min}} * (\mathcal{P}_a\mathbf{E}_0)]\tilde{\phi} - \hat{\mathcal{P}}_{k_{\min}} * (\mathcal{P}_a\mathbf{E}_0\tilde{\phi})\right\} \quad (18)$$

to first order in $\tilde{\phi}$ for constant polarization of $\mathbf{E}_0$. The first two terms of (18) represent the DC signal originating from the PCI laser beam, which is important for determining the noise level observed by the PCI detectors, while the last term is proportional to $\tilde{\phi}$ and contains the information related to $\tilde{n}_e$. Inserting $|T * \mathbf{E}_a|^2$ from (18) in (15), with $\mathbf{E}_0$ from (1), and writing $P_{\rm det} = P_{\rm det}^{\rm DC} + \tilde{P}_{\rm det}$, where $P_{\rm det}^{\rm DC}$ is the DC power on the detector element and $\tilde{P}_{\rm det}$ is the power modulation proportional to $\tilde{\phi}$, we find

$$P_{\rm det}^{\rm DC} = \frac{2P_0}{\pi W_0^2}\int_{M\times{\rm det}} \mathrm{e}^{-2y^2/W_0^2}\left[|\mathcal{P}_a\,\mathrm{e}^{-x^2/W_0^2} - \hat{\mathcal{P}}_{k_{\min}} * (\mathcal{P}_a\,\mathrm{e}^{-x'^2/W_0^2})|^2 + \rho\,|\hat{\mathcal{P}}_{k_{\min}} * (\mathcal{P}_a\,\mathrm{e}^{-x'^2/W_0^2})|^2\right]\mathrm{d}\mathbf{x}_\perp, \quad (19)$$

$$\tilde{P}_{\rm det} = \frac{4\sqrt{\rho}P_0}{\pi W_0^2}\int_{M\times{\rm det}} \mathcal{P}_a\,\mathrm{e}^{-(x^2+2y^2)/W_0^2}\left\{[\hat{\mathcal{P}}_{k_{\min}} * (\mathcal{P}_a\mathrm{e}^{-x'^2/W_0^2})]\tilde{\phi} - \hat{\mathcal{P}}_{k_{\min}} * (\mathcal{P}_a\mathrm{e}^{-x'^2/W_0^2}\tilde{\phi})\right\}\mathrm{d}\mathbf{x}_\perp; \quad (20)$$

the convolution integrals in (19) and (20) may be evaluated by inserting $\hat{\mathcal{P}}_{k_{\min}}$ and $\mathcal{P}_a$,

$$[\hat{\mathcal{P}}_{k_{\min}} * (\mathcal{P}_a g)](\mathbf{x}_\perp) = \int_{-\sqrt{a^2-y^2}}^{\sqrt{a^2-y^2}} \frac{\sin[k_{\min}(x-x')]}{\pi(x-x')} g(x',y)\,\mathrm{d}x'. \quad (21)$$

To show that (19) and (20) possess the basic properties expected of a PCI diagnostic, we note that $\hat{\mathcal{P}}_{k_{\min}} \to \delta$ when convolved with a function whose k_x-spectrum is dominated by components with $|k_x| \ll k_{\min}$. Since this is generally true for $\mathcal{P}_a\,\mathrm{e}^{-x'^2/W_0^2}$ when $k_{\min}W_0, k_{\min}a \gg 1$, (19) can be written as $P_{\rm det}^{\rm DC} \approx [2\rho P_0/(\pi W_0^2)]\int_{M\times{\rm det}} \mathcal{P}_a\,\mathrm{e}^{-2x_\perp^2/W_0^2}\,\mathrm{d}\mathbf{x}_\perp$, which is the value expected when the unscattered Gaussian beam spot is fully contained in the phase plate groove and diffraction effects are ignored. If the k_x-spectrum of $\tilde{\phi}$ is further dominated by components with $|k_x| \ll k_{\min}$, such that we can let $\hat{\mathcal{P}}_{k_{\min}} \to \delta$ in the convolution with $\mathcal{P}_a\,\mathrm{e}^{-x'^2/W_0^2}\tilde{\phi}$, it holds from (20) that $\tilde{P}_{\rm det} \approx 0$, illustrating the expected cutoff of low-$|k_x|$ fluctuations due to the phase plate.

2.1. Detector response and noise

The output given by the PCI detectors is a convolution of $P_{\rm det}$ with an instrument response function, H, whose temporal Fourier transform is given by

$$\hat{H}(f) = \frac{H_0}{\sqrt{(1+f_h^2/f^2)(1+f^2/f_l^2)}}, \quad (22)$$

with f being the frequency, while the high-pass frequency, $f_h = 2\,\mathrm{kHz}$, the low-pass frequency, $f_l = 623\,\mathrm{kHz}$ (or $507\,\mathrm{kHz}$), and the peak responsivity, $H_0 = 16.4\,\mathrm{kV/W}$ (or $9.05\,\mathrm{kV/W}$), are representative of the photoconductive HgCdTe detector arrays and preamplifiers at W7-X [24]. Since the frequency dependence of the detector response

is already corrected for in the processed experimental data, we generally consider the detector output to be given by $H_0 P_{\mathrm{det}}$. The signal of interest to PCI is $\tilde{S} = H_0 \tilde{P}_{\mathrm{det}}$, but the full (AC) signal, S, also contains a noise component, S_{noise}, such that $S = \tilde{S} + S_{\mathrm{noise}}$. We consider a simple noise model, including only laser shot noise and thermal noise, with both noise signals taken as white, Gaussian, and additive. Under these assumptions, the root mean square value of the signal associated with the noise is given by [28, 57]

$$S_{\mathrm{noise}}^{\mathrm{rms}} = H_0 \sqrt{\Delta f} \sqrt{\frac{4hcP_{\mathrm{det}}^{\mathrm{DC}}}{\eta \lambda_0} + \frac{A_{\mathrm{det}}}{D^{*2}}}, \tag{23}$$

where h is the Planck constant, c is the speed of light, Δf is the detector bandwidth, η is the detector quantum efficiency at λ_0, A_{det} is the detector element area, and D^* is the detector thermal detectivity. Here, we use the parameters $\Delta f = 2\,\mathrm{MHz}$, $A_{\mathrm{det}} = W_{\mathrm{det}} h_{\mathrm{det}} = 0.5\,\mathrm{mm}^2$, $\eta = 0.02$, and $D^* = 4.8 \times 10^{10}\,\mathrm{cm}\sqrt{\mathrm{Hz}}/\mathrm{W}$ (or $3.4 \times 10^{10}\,\mathrm{cm}\sqrt{\mathrm{Hz}}/\mathrm{W}$) for the liquid nitrogen cooled photoconductive HgCdTe detectors at W7-X. The detector noise is modeled by adding random numbers following a Gaussian distribution with a mean of 0 and a standard deviation of $S_{\mathrm{noise}}^{\mathrm{rms}}$ from (23) to $\tilde{S}$ for each detector element.

2.2. Calibration

We now discuss the problem of obtaining a calibrated synthetic PCI signal through a known sound wave signal produced by a calibration speaker located along the PCI beam line, in order to mimic the experimental calibration technique [24, 54]. As shown in Appendix A, a sound wave in the standard atmosphere producing a perturbed line-integrated pressure field along the PCI LoSs, $\int_{\mathrm{LoS}} \tilde{p}\,\mathrm{d}z$, may be modeled by inserting an equivalent line-integrated perturbed electron density along the PCI LoSs of

$$\left(\int_{\mathrm{LoS}} \tilde{n}_e\,\mathrm{d}z \right)_{\mathrm{cal}} = -\frac{2\pi(N_0 - 1)}{r_e \lambda_0^2 \gamma p_0} \int_{\mathrm{LoS}} \tilde{p}\,\mathrm{d}z, \tag{24}$$

where $\gamma = 1.4$ is the adiabatic index of dry air at 293 K, $p_0 = 101.325\,\mathrm{kPa}$ is the standard atmospheric pressure, and $N_0 - 1 = 2.726 \times 10^{-4}$ is the deviation of the refractive index of the standard atmosphere from 1 [31]. We note that (24) has the same absolute value as the result from [31], but opposite sign. The linear fit of the root mean square $\int_{\mathrm{LoS}} \tilde{p}\,\mathrm{d}z$ to x from [54] is used to represent a typical calibration signal at W7-X. This gives the following instantaneous $\int_{\mathrm{LoS}} \tilde{p}\,\mathrm{d}z$,

$$\int_{\mathrm{LoS}} \tilde{p}\,\mathrm{d}z = K(1 - Cx) \cos\left[2\pi f_s \left(\frac{x}{v_s} - t \right) + \Phi \right], \tag{25}$$

where $K = 0.55\,\mathrm{Pa} \cdot \mathrm{m}$, $C = 3.2\,\mathrm{m}^{-1}$, $v_s = 343\,\mathrm{m/s}$ is the speed of sound in dry air at 293 K, f_s is the frequency of the sound wave, t is time, and Φ is the phase of the sound wave at $x, t = 0$. The calibration signal leads to spectra peaked around $f = f_s$ and $k_x = k_s = 2\pi f_s / v_s$ in Fourier space. When $k_s > k_{\mathrm{min}}$, this enables a calibration to be established between $\tilde{S}$ and $\int_{\mathrm{LoS}} \tilde{n}_e\,\mathrm{d}z$ for $|k_x| > k_{\mathrm{min}}$ [24, 54], cf. Appendix A.

2.3. Numerical Implementation

In order to perform investigations using the synthetic PCI diagnostic described above, a numerical implementation is required. This is done using Python3, allowing the synthetic PCI diagnostic to interface smoothly with the packages used for analyzing experimental PCI data, the W7-X magnetic field geometry, and W7-X plasma profiles. As input, we take $\int_{\mathrm{LoS}} \tilde{n}_e \,\mathrm{d}z$ on a rectangular grid in the (x, y)-plane; the calculation of $\int_{\mathrm{LoS}} \tilde{n}_e \,\mathrm{d}z$ from gyrokinetic simulations is discussed in Section 3. The center of detector element 16 is defined as the origin in the (x, y)-plane and each detector element is assumed to cover a rectangle with side lengths MW_{det} and Mh_{det} along the x- and y-directions, respectively, in the plasma. A variable number of grid points may be used along the x and y directions. In this paper, we use an x-grid with 273 evenly spaced points covering $x \in [-a, a]$ and a y-grid with three evenly spaced points covering $y \in [-Mh_{\mathrm{det}}/2, Mh_{\mathrm{det}}/2]$ for $\int_{\mathrm{LoS}} \tilde{n}_e \,\mathrm{d}z$, which is found to be sufficient for convergence. The convolutions required for evaluation of (19) and (20) are computed using the convolve function of SciPy, and the integrals over the detector elements are performed numerically using Simpson's formula to obtain $\tilde{S}$ and $P_{\mathrm{det}}^{\mathrm{DC}}$. The integrals and convolutions are done on a grid with 100 times higher resolution along the x-direction to obtain an accurate representation of the detector areas; $\int_{\mathrm{LoS}} \tilde{n}_e \,\mathrm{d}z$ is interpolated to the new grid using cubic splines. Model noise can be included by generating a Gaussian distribution of random numbers with zero mean and a standard deviation given by (23) for each detector element, using the random.normal function of NumPy.

To illustrate the results obtained using the numerical implementation of the synthetic PCI diagnostic, figure 2 shows the DC power on each detector element, computed by evaluating (19) with the scheme described above. In the left pane of figure 2, and in the rest of the paper unless explicitly stated otherwise, the parameters $P_0 = 6.3\,\mathrm{W}$, $M = 5$, $W_0 = 4\,\mathrm{cm}$, and $a = 6.8\,\mathrm{cm}$, representative of the previous W7-X operation phases, are utilized. Evidently, the diffraction effects and integration over the detector elements described by (19) only introduce small deviations from the initial Gaussian beam shape in the region covered by the detector elements in this case. The right pane of figure 2 shows the results when $a = 4.2\,\mathrm{cm}$ is used while keeping all other parameters constant. This value of a is representative of future W7-X operation phases, due to the installation of additional port liner to enable long-pulse operation. In the $a = 4.2\,\mathrm{cm}$ case, significant deviations of the beam pattern from a Gaussian due to diffraction are observed, since the images of the outer detector elements now extend to regions with $|x| \gtrsim a$. We particularly note that $P_{\mathrm{det}}^{\mathrm{DC}} = 0$ at the final detector element, due to it exclusively covering regions with $x > a$ for $M = 5$. This indicates that it will be desirable to use smaller values of M in future W7-X operation phases in order to minimize diffraction and beam clipping effects.

Additional verification that the synthetic PCI diagnostic produces accurate results is provided by computing the calibration signal expected based on (24) with $\int_{\mathrm{LoS}} \tilde{p} \,\mathrm{d}z$ from (25) for $f_s = 20\,\mathrm{kHz}$ and $\Phi = 0$. The basic $\tilde{S}_{\mathrm{cal}}$, calculated based on the numerical

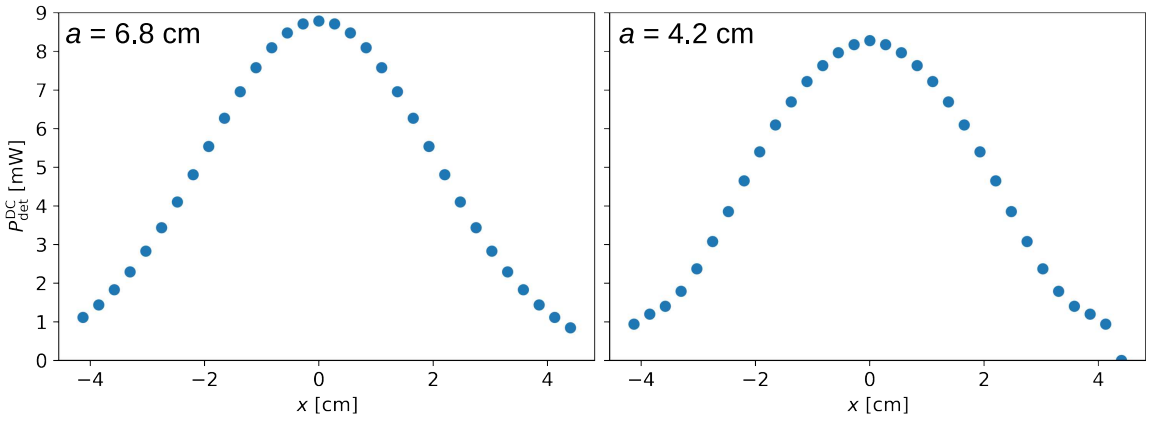

Figure 2. $P_{\mathrm{det}}^{\mathrm{DC}}$ from (19) on each detector element calculated using the numerical implementation of the synthetic PCI diagnostic with $P_0 = 6.3\,\mathrm{W}$, $M = 5$, and $W_0 = 4\,\mathrm{cm}$. The left pane has $a = 6.8\,\mathrm{cm}$, representative of the previous W7-X operation phases. The right pane has $a = 4.2\,\mathrm{cm}$, representative of future W7-X operation phases.

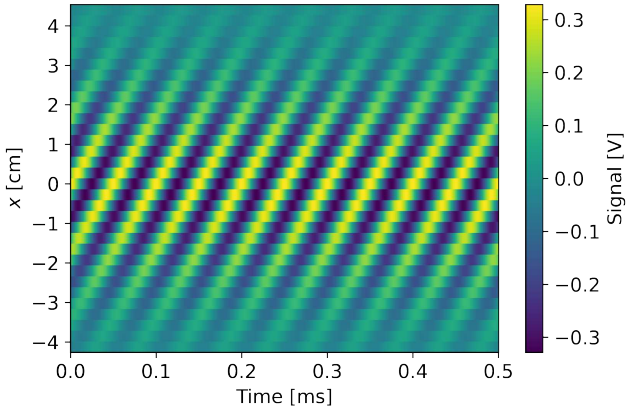

Figure 3. Synthetic calibration signal obtained by application of the numerical implementation of the synthetic PCI diagnostic to $(\int_{\mathrm{LoS}} \tilde{n}_e \,\mathrm{d}z)_{\mathrm{cal}}$ from (24) with $\int_{\mathrm{LoS}} \tilde{p}\,\mathrm{d}z$ from (25) for $f_s = 20\,\mathrm{kHz}$ and $\Phi = 0$.

implementation of (20) for $t \in [0, 0.5\,\mathrm{ms}]$ with a time resolution of $0.5\,\mu\mathrm{s}$, is seen in figure 3; the plot of S_{cal} including noise looks essentially identical and is not shown. From figure 3, structures with a temporal period of 0.05 ms and a spatial period of 1.7 cm are readily identified and seen to propagate in the positive x-direction at approximately 340 m/s. The above characteristics are as expected for the sound wave, which has $1/f_s = 0.05\,\mathrm{ms}$, $\lambda_s = v_s/f_s = 1.7\,\mathrm{cm}$, and $v_s = 343\,\mathrm{m/s}$. The synthetic calibration signal of figure 3 is additionally found to resemble the experimental one from figure 7 of [24], both in terms of shape and signal amplitude. To analyze the more complicated synthetic PCI signals associated with plasma turbulence, it is usually advantageous to compute the power spectral density (psd) in (k_x, f)-space in a manner similar to what is done for the experimental observations [24, 25]. For the remainder of this paper, we drop the x-subscript and denote k_x by k, as is costumary in the PCI literature. The psd in (k, f)-

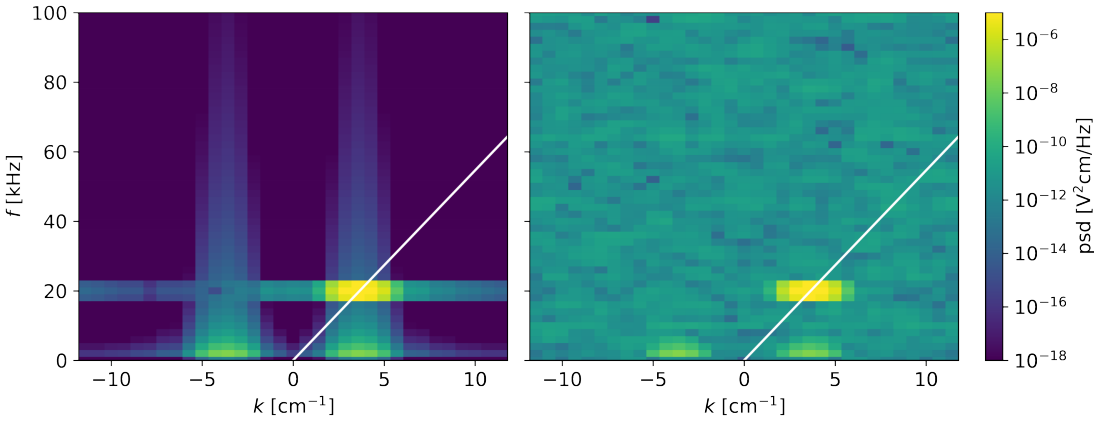

Figure 4. Synthetic (k, f)-spectra based on the synthetic calibration signal from figure 3. The left pane shows the signal without model noise included, while the right pane includes noise. In both cases, a strong peak is observed around $f = f_s$ and $k = k_s$, giving $v_{\mathrm{ph}} = 2\pi f_s/k_s = v_s$ (shown by the white lines), as expected.

space computed from $\tilde{S}_{\mathrm{cal}}$ of figure 3 is seen in the left pane of figure 4, while the psd including noise is seen in the right pane of figure 3 (in both cases, only $f \in [0, 100\,\mathrm{kHz}]$ is shown). In agreement with the structures observed in figure 3, both (k, f)-spectra in figure 4 have a large peak near $f = f_s = 20\,\mathrm{kHz}$ and $k = k_s = 2\pi f_s/v_s = 3.66\,\mathrm{cm}^{-1}$; the fact that the peak occurs for $k > 0$ additionally indicates propagation in the positive x-direction, as expected. The inclusion of model noise in the right pane of figure 4 is seen to obscure most spectral features away from the main peak that are present in the left pane, indicating that only the main peak and some low-frequency features near $k = \pm k_s$ are expected to be observable experimentally, which is indeed the case, cf. figure 8 of [24]. Using the method outlined in [25], we are further able to infer a PCI phase velocity, $v_{\mathrm{ph}} = 2\pi f_s/k_s$, shown by the white lines in figure 4, which matches v_s, demonstrating that the synthetic PCI diagnostic accurately captures the velocity of the underlying fluctuations even in the presence of detector noise, as expected [25]. We have thus verified that the synthetic PCI diagnostic is capable of reproducing a calibration signal resembling the experimental one, indicating that the numerical implementation is successful. Additional discussion of the validity of the implemented instrument response is presented in Section 3.

3. Implementation of global, nonlinear gyrokinetic turbulence models

Now that the basic features of the synthetic PCI diagnostic developed for turbulence studies at W7-X have been described, we turn to the issue of computing $\tilde{\phi}$ based on global, nonlinear gyrokinetic codes, specifically GENE-3D [47–50] and EUTERPE [51]. As the simulations analyzed in this section do not include the effect of a neoclassical radial electric field, which plays a dominant role in determining the experimental v_{ph} [25] and can have a strong effect on the saturation level of ITG turbulence [53], the results

should not be considered to represent experimental PCI data directly. Instead, we focus on four main goals. 1) to describe the steps involved in integrating global, nonlinear gyrokinetic codes with the synthetic PCI diagnostic, including the analysis techniques used to interpret the results provided by the synthetic PCI diagnostic. 2) to compare the k-spectra of the synthetic PCI signals from the different simulations with various models [16, 58–63]. 3) to identify potential universal features of global, nonlinear gyrokinetic simulations of W7-X using specific approximations, e.g., adiabatic electrons, in the PCI spectral range. 4) to confirm that the synthetic PCI signals provide an accurate representation of the features of the underlying $\int_{\mathrm{LoS}} \tilde{n}_e \, \mathrm{d}z$.

The PCI LoSs are taken to be straight lines between the ports shown in [24], and are indicated in figures 1 and 5. The positions of the LoSs are computed in PEST coordinates [64] for a given magnetic configuration using the VMEC code [65]. PEST coordinates were originally introduced by a tokamak magnetohydrodynamic stability code of the same name [64] and parameterize closed flux surfaces of toroidal systems by three coordinates, ψ, φ, and θ^*. ψ is a normalized radial coordinate related to the toroidal magnetic flux, Ψ, through a flux surface; here, we define $\psi = \sqrt{\Psi/\Psi_{\mathrm{LCFS}}}$, where Ψ_{LCFS} is Ψ at the last closed flux surface, such that ψ is 0 on the magnetic axis, 1 on the last closed flux surface, and roughly proportional to the effective distance from the magnetic axis. φ is the usual cylindrical toroidal angle. θ^* is a poloidal angle-like coordinate, chosen such that magnetic field lines are straight in (φ, θ^*)-space and increments of 2π in θ^* correspond to the same position [64] (this means that a part of a flux surface covering $\theta^* \in [\theta_0^*, \theta_0^* + \Delta\theta^*]$ contains a toroidal magnetic flux of $[\Delta\theta^*/(2\pi)]\Psi$ independent of θ_0^* [64]). Since GENE-3D visualizations are done on a regular grid in PEST coordinates [47–50] and EUTERPE utilizes a regular PEST coordinate grid directly in the simulation [51], this representation is convenient for fast interpolation. Because the PCI LoSs cover $\varphi \in [4.53, 4.57]$ and the signal is sampled at a rate of 2 MHz in W7-X [24], it is further possible to utilize only a small part of the simulation output for the synthetic PCI diagnostic calculations. As both GENE-3D and EUTERPE are δf codes, $\tilde{n}_e$ can be extracted directly from the simulations on the PEST grids and thereupon interpolated to the PCI LoSs, allowing the calculation of $\tilde{\phi}(\mathbf{x}_\perp, z)$ through cumulative numerical integration using the trapezoid method for 2000 evenly spaced points along each LoS; after the computation, a smaller number of points, generally 200, along the LoSs are saved to enable investigations of the radial regions giving rise to the various features of $\tilde{S}$.

3.1. GENE-3D

We first discuss the results obtained by applying the synthetic PCI diagnostic to simulations performed using the GENE-3D code. GENE-3D is an Eulerian code extending the well-known GENE family of codes to allow global, nonlinear simulations of non-axisymmetric magnetic configurations, with a particular focus on the geometry of W7-X. Several GENE-3D benchmarks and runs have been performed, as discussed

Simulation Case	min(ψ)	max(ψ)	t-Resolution [μs]	t-Interval [μs]
GENE-3D Low-β KE	0.3	0.7	0.48	123.61
GENE-3D Low-β AE	0.3	0.7	4.07	83.91
GENE-3D Standard [49]	0.1	0.9	4.33	1432.60
EUTERPE [51]	0.04	0.45	0.64	350.12

Table 1. Basic parameters of the $\tilde{n}_e$-profiles extracted from the global, nonlinear gyrokinetic simulations investigated in the present paper.

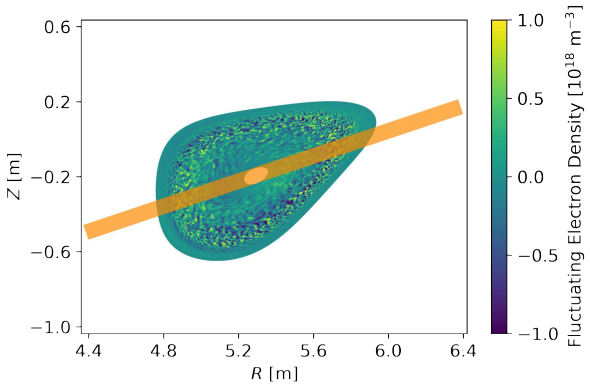

Figure 5. Poloidal slice of W7-X near the center of the PCI LoSs ($\varphi = 4.55$); (R, Z) are cylindrical coordinates. The LoSs are marked by the orange shaded area, while $\tilde{n}_e$ from single time point of the GENE-3D simulation from [49] is displayed in the background.

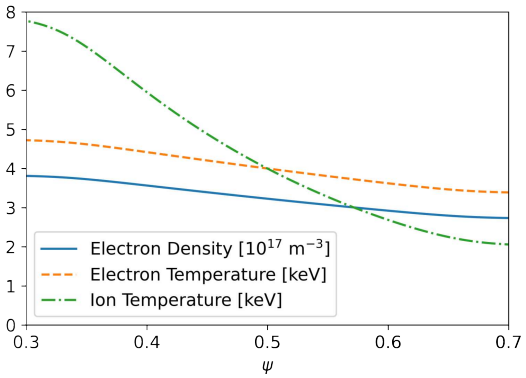

Figure 6. Background electron density (solid line), electron temperature (dashed line), and ion temperature (dash-dotted line) profiles of the low-β simulations versus ψ.

in [47–50]. The runs discussed in connection with the synthetic PCI diagnostic are the adiabatic electron (AE) simulation of the W7-X standard configuration from [49] and two more recent very low-β simulations of the W7-X standard configuration, similar to the ones studied in [50]; one of the low-β simulations includes kinetic electrons (KEs), while the other one uses AEs for comparison. The basic parameters of the extracted $\tilde{n}_e$-profiles are seen in table 1. Additionally, the background electron density, electron

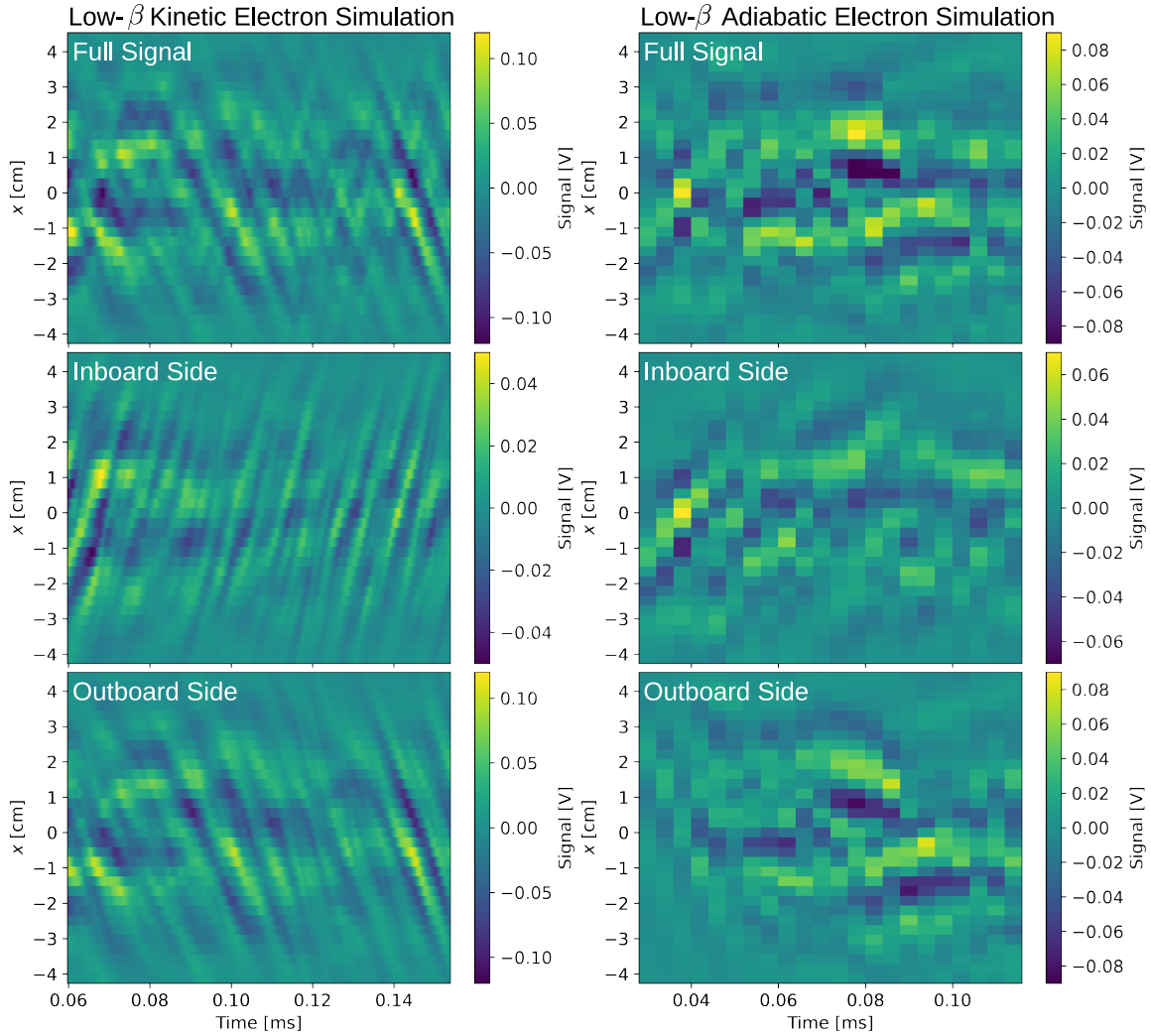

Figure 7. Synthetic PCI signal based on low-β GENE-3D simulations with KEs (left column) and AEs (right column). The top panes show $\tilde{S}$ obtained by integrating $\tilde{n}_e$ over the full LoSs, while the middle and bottom panes show $\tilde{S}$ obtained by integration over only the inboard and outboard sides, respectively.

temperature, and ion temperature profiles of the low-β simulations are shown in figure 6 (the background ion density is identical to the electron density, as only protium ions are considered in all cases); a similar plot for the AE simulation from [49] is found in figure 2 of [49]. As is evident from table 1, each run has some unique features. The AE simulation from [49] covers the range $\psi \in [0.1, 0.9]$, but has a relatively low temporal resolution, making it good for studying global effects and less ideal for obtaining specific spectral features. The low-β simulations on the other hand only cover the radial range of $\psi \in [0.3, 0.7]$, but the KE simulation has a time resolution close to $0.5\,\mu$s, making it less suitable for studying global effects, but well suited for looking into specific spectral features; the low-β AE simulation has a time resolution similar to that of the simulation from [49] and is mainly useful for illustrating the difference between AE and KE simulations.

3.1.1. PCI signals and rotation direction Figure 7 shows $\tilde{S}$ obtained from the synthetic PCI diagnostic with $P_0 = 6.3\,\mathrm{W}$, $M = 5$, $W_0 = 4\,\mathrm{cm}$, and $a = 6.8\,\mathrm{cm}$ for the low-β KE and AE simulations in the left and right hand columns, respectively. Specifically, the top panes of figure 7 display $\tilde{S}$ when $\tilde{n}_e$ is integrated over the full LoSs, indicating that structures propagating in both the positive and negative x-direction are present. In order to gain insight into the plasma rotation direction, the middle and bottom panes of figure 7 show $\tilde{S}$ when $\tilde{n}_e$ is integrated over the inboard and outboard sides of W7-X, respectively; the inboard and outboard sides are defined as the regions along each LoS for which ψ is, respectively, decreasing and increasing as a function of z, which roughly corresponds to the regions left and right of the plasma center in figure 5. Evidently, the structures mainly propagate in the positive x-direction on the inboard side and the negative x-direction on the outboard side for the KE simulation, as well as during the initial part of the AE simulation. This corresponds to a dominant rotation in the electron diamagnetic direction, which is the propagation direction of linear TEMs and ETG modes, while linear ITG modes propagate in the opposite (ion diamagnetic) direction. As both simulations only cover ITG scales and neither of them include modifications of the rotational velocity due to a neoclassical radial electric field, E_r, the fact that the turbulent structures are able to propagate in the electron diamagnetic direction may seem somewhat counter intuitive. We do, however, note that the rotational velocity observed in the simulation is mainly determined by nonlinearly generated zonal flows, whose direction need not have any relation to that of the underlying linear modes, meaning that such a reversal is possible; a similar result was obtained based on an AE simulation from the EUTERPE code [51] in [45]. Further supporting this interpretation, the rotation direction is seen to change sign in parts of the plasma on a time scale $\sim 300\,\mu\mathrm{s}$ in the AE simulation of the W7-X standard configuration from [49]. In the AE simulation of figure 7, only an early indication of a change of the rotational velocity is visible toward the end of the time simulated, owing to the short length of the simulated time interval, cf. table 1. These observations clearly illustrate that care must be taken when attempting to apply results from linear theory to nonlinear simulations and experimental results. A final observation regarding figure 7 is that the signal from the outboard side attains a larger amplitude than that from the inboard side in both simulations, as generally expected for toroidal plasmas.

3.1.2. (k,f)-spectra and PCI phase velocity In order to quantify the plasma rotation indicated by figure 7, we plot the associated (k, f)-spectra in figure 8. The (k, f)-spectra are in agreement with expectations from figure 7. We also note the reduced psd at $|k| < k_{\min}$ in all cases, which is related to the low-$|k|$ cutoff introduced by the PCI phase plate, further verifying the implementation of the synthetic PCI diagnostic. When integrating over the full LoSs, branches displaying both positive and negative $v_{\mathrm{ph}} = 2\pi f/k$ are visible for both simulations. Restricting the integrals to the inboard and outboard sides leaves mainly the branch with $v_{\mathrm{ph}} > 0$ for the inboard side and the branch with $v_{\mathrm{ph}} < 0$ for the outboard side, respectively, which is in agreement with the

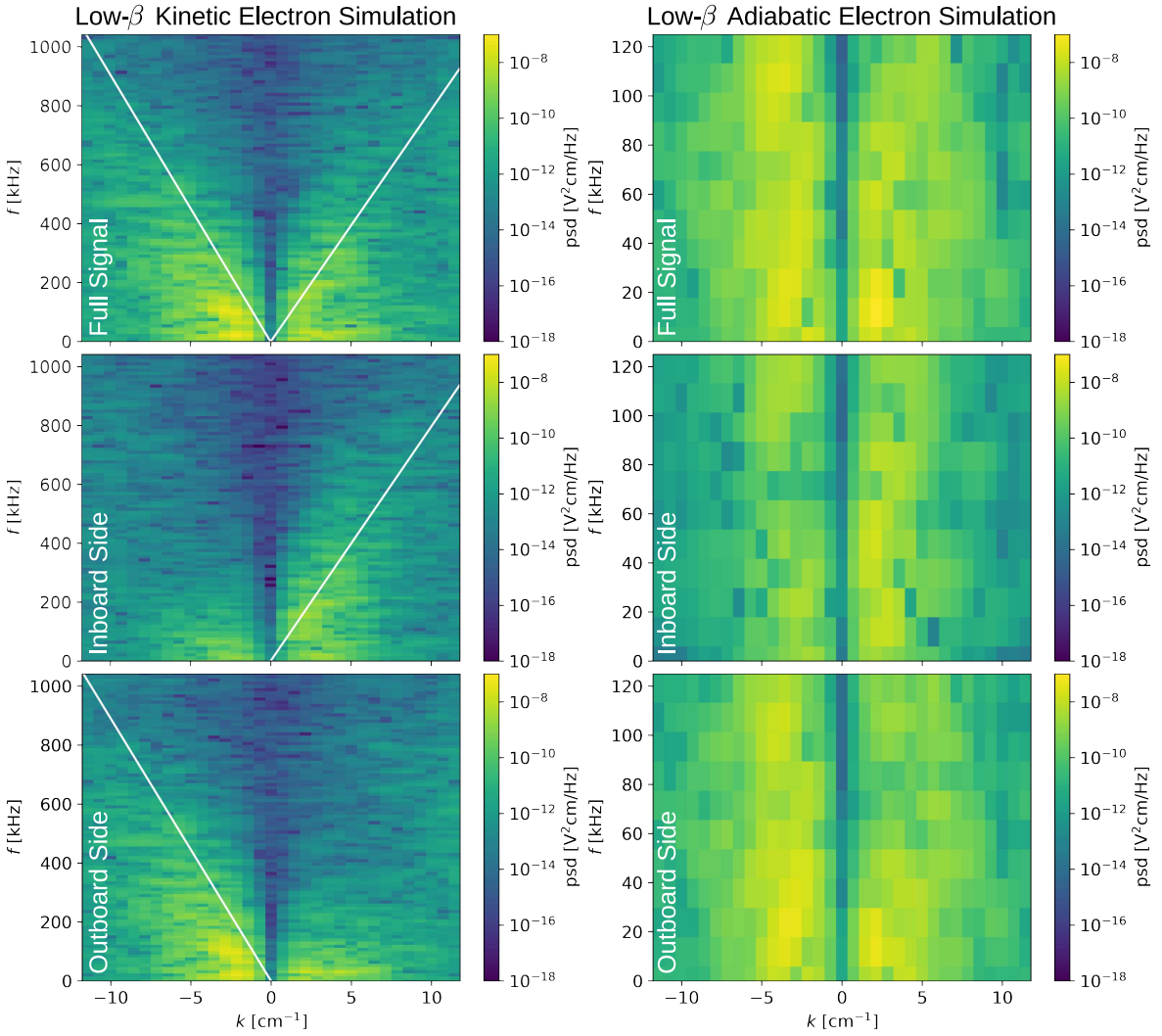

Figure 8. Synthetic (k, f)-spectra based on GENE-3D simulations with KEs (left column) and AEs (right column). The top panes show the (k, f)-spectra obtained by integrating $\tilde{n}_e$ over the full LoSs, while the middle and bottom panes show the (k, f)-spectra obtained by integration over only the inboard and outboard sides, respectively. The white lines in the KE cases indicate the v_{ph}-values obtained by the method of [25].

rotation direction found in figure 7. We also note that most of the psd originates from the outboard side, which is again in agreement with figure 7. The magnitude of v_{ph} may be estimated for the KE simulation using the method described in [25], while the low temporal resolution of the AE simulation, coupled with the non-constant velocity observed for it in figure 7, makes such an estimate difficult in that case. In the KE case, the method of [25] yields $v_{\mathrm{ph}} = 4.9\,\mathrm{km/s}$ and $-5.7\,\mathrm{km/s}$ for integration over the full LoSs, while $v_{\mathrm{ph}} = 5.0\,\mathrm{km/s}$ for integration over the inboard side and $v_{\mathrm{ph}} = -5.6\,\mathrm{km/s}$ for integration over the outboard side; these v_{ph}-values are illustrated by the white lines in figure 8. The closeness of the positive and negative v_{ph}-values obtained from the full LoSs to those obtained from integration over the inboard and outboard sides, respectively, further justifies the identification of each v_{ph}-branch with the respective

plasma region. We additionally note that the inclusion of the model detector noise described in Subsection 2.1 only leads to small changes of the computed v_{ph}, which was also the case in figure 4 and in agreement with [25]. While the v_{ph}-values inferred from figure 8 are similar to those observed experimentally in ECRH plasmas at W7-X [25], we note that the lack of inclusion of a neoclassical E_r, which is expected to dominate the experimental rotational velocity [25], means that this correspondence is most likely spurious and originates from the unrealistic plasma parameters used in the KE simulation, seen in figure 6.

3.1.3. k-spectra and comparison with theoretical models We next examine the k-spectra obtained by applying the synthetic PCI diagnostic to the GENE-3D simulations and compare them with various models [16, 58–63]. The k-spectra of the low-β GENE-3D simulations, obtained by integrating the psd from the (k, f)-spectra covering the full LoSs in figure 8 over the interval $f \in [0, 600\,\mathrm{kHz}]$ and averaging over values with the same $|k|$, are seen in the top row of figure 9. The bottom row of figure 9 shows the same quantities obtained from (k, f)-spectra including noise based on the model of Subsection 2.1. As expected for turbulent k-spectra, the psd of the k-spectra in figure 9 may be approximated by power laws (functions of the type $A|k|^{\alpha}$, where $A, \alpha \in \mathbb{R}$) with different exponents in different k-regions. The exponents obtained from least-square fits to power laws in the different k-regions are also indicated in figure 9, along with uncertainties given by the standard errors of the fits. Evidently, the k-spectra obtained from the simulations with KEs and AEs follow distinct power laws with different exponents in different regions of k-space, although we note that the exponents become more negative for larger $|k|$ in both cases.

In the KE case, the k-spectrum follows a power law with an exponent of -3.1 ± 0.3 from $|k|$ slightly above k_{min} (shown in figure 9 for reference) to $|k| = 5.7\,\mathrm{cm}^{-1}$ and a power law with an exponent of -6.1 ± 0.3 above $|k| = 5.7\,\mathrm{cm}^{-1}$. When noise is included, the exponent for $|k| < 5.7\,\mathrm{cm}^{-1}$ remains close to -3, while the exponent for $|k| > 5.7\,\mathrm{cm}^{-1}$ is modified to -4.8 ± 0.5, meaning that the k-spectrum is less steep at low psd, as expected since the noise is approximately white in k-space. The exponents in the KE case are similar to those observed by CO_2 laser scattering at the Tore Supra tokamak [16] and also appear compatible with a turbulence model of the form $A|k|^{-3}/(1 + \rho_s^2|k|^2)^2$ proposed by [62], where ρ_s is the hybrid thermal ion Larmor radius. The transition between the two exponents occurs at $|k| = 5.7\,\mathrm{cm}^{-1}$ which is similar to $1/\rho_s \approx 4\,\mathrm{cm}^{-1}$ in the simulation, as expected from [62]; the variation of ρ_s over the domain of the low-β simulations is small due to the flat electron temperature profile, seen in figure 6, and the large aspect ratio of W7-X, which leads to a small variation of the background magnetic field strength. We do, however, note that extending the k-range by reducing M yields a region with an exponent of -4.4 ± 0.6 for $|k| > 13.1\,\mathrm{cm}^{-1}$, rather than the expectations of an exponent close to -7 from [62]. This may be a result of the high-$|k|$ modes being poorly resolved due to the finite difference scheme used in the simulation.

In the AE case, three distinct power laws are found in figure 9. From $|k|$ slightly

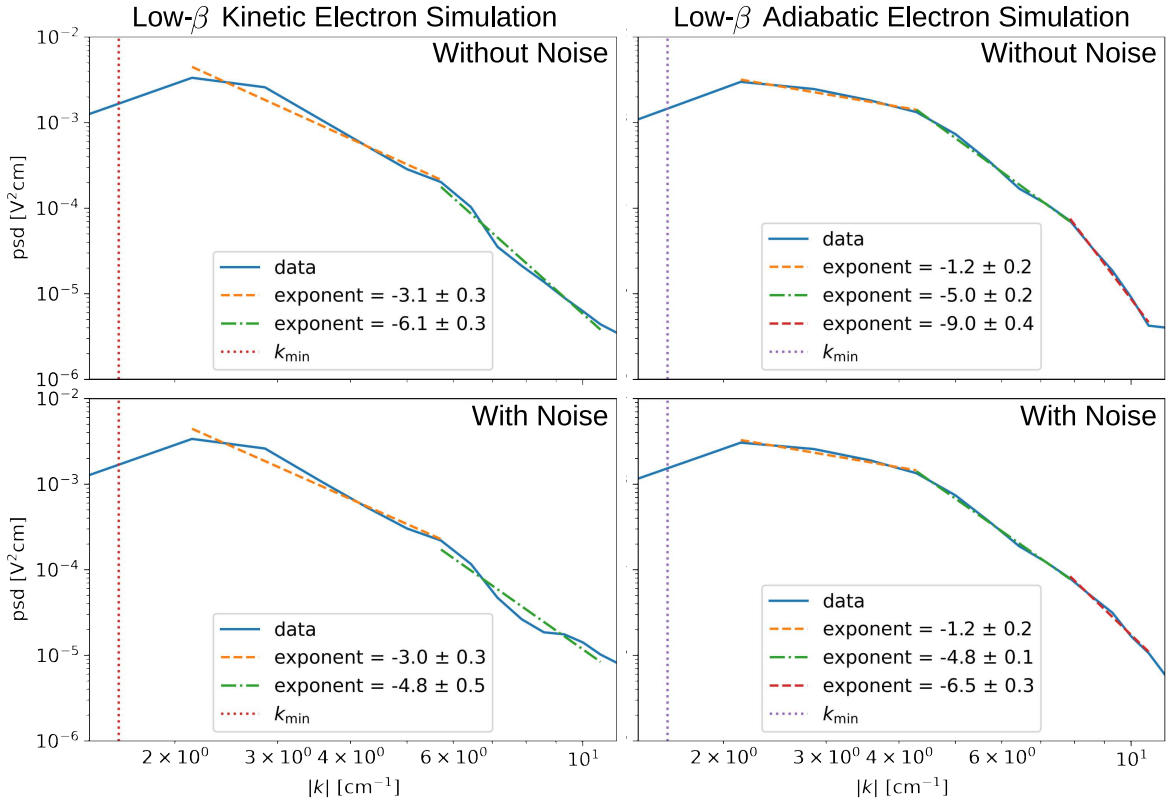

Figure 9. Synthetic k-spectra based on low-β GENE-3D simulations with KEs (left column) and AEs (right column), along with power law fits. The top and bottoms rows show k-spectra without and with the inclusion model noise, respectively.

above $k_{\min}$ to $4.3\,\mathrm{cm}^{-1}$, an exponent of -1.2 ± 0.2 is found, while an exponent of -5.0 ± 0.2 is found for $|k| \in [4.3\,\mathrm{cm}^{-1}, 7.9\,\mathrm{cm}^{-1}]$, and finally for $|k| > 7.9\,\mathrm{cm}^{-1}$, an exponent of -9.0 ± 0.4 is found; the flattening at $|k| > 10\,\mathrm{cm}^{-1}$ is due to aliasing. The inclusion of noise only significantly changes the exponent for $|k| > 7.9\,\mathrm{cm}^{-1}$ (from -9.0 ± 0.4 to -6.5 ± 0.3) and again leads to a less steep k-spectrum at low psd due to the noise being approximately white in k-space. The transition from an exponent of -1.2 ± 0.2 to -5.0 ± 0.2 occurs near $1/\rho_s$ and is consistent with turbulent energy being injected around this scale, as expected for ITG modes. An exponent of -5 further matches probe measurements from the Étude stellarator [58], predictions for drift wave turbulence with AEs from [59, 60, 63], the nonlinear ITG simulation of [61], and previous results for AE simulations with GENE-3D and EUTERPE, obtained using the synthetic PCI diagnostic at W7-X [45]. The transition from an exponent of -5.0 ± 0.2 to -9.0 ± 0.4 has a less clear interpretation, but is likely related to an unrealistically high damping rate of high-$|k|$ modes induced by the hyper-diffusion term included to improve the stability of the numerical scheme employed by GENE-3D [47,48], in analogy with the synthetic Doppler reflectometry observations of [14]. To check whether such a transition occurs in other GENE-3D simulations with AEs, we plot the k-spectrum obtained from the simulation of the W7-X standard configuration of [49] in figure 10. The k-spectra in figure 10 have

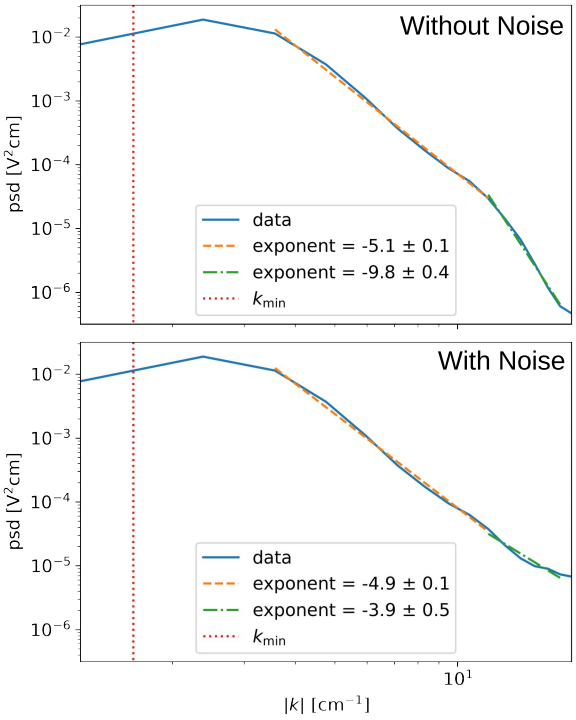

Figure 10. Synthetic k-spectra based on the GENE-3D simulation of the W7-X standard configuration with AEs from [49], along with power law fits. The top and bottoms panes show k-spectra without and with the inclusion of model noise, respectively. To investigate the spectra at high k, we have used $M = 3$.

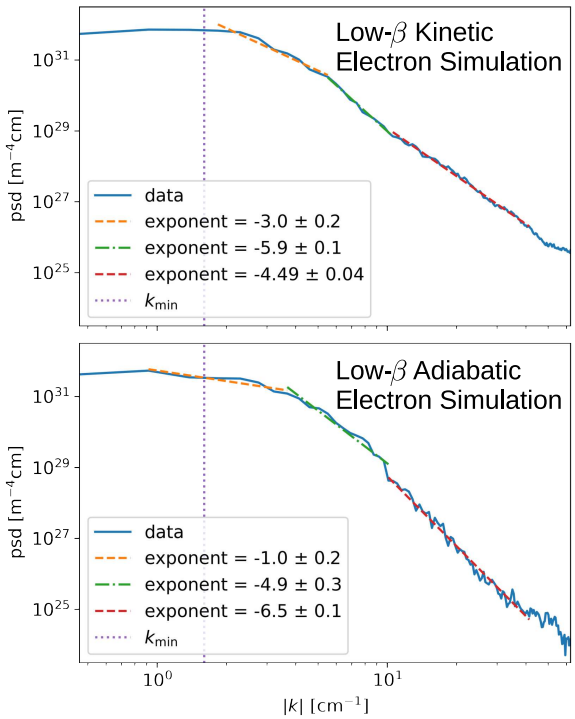

Figure 11. Synthetic k-spectra of $\int_{\mathrm{LoS}} \tilde{n}_e \, \mathrm{d}z$ based on the low-β GENE-3D simulations with KEs (top pane) and AEs (bottom pane), along with power law fits.

been computed using $M = 3$, rather than the value of 5 used in the rest of this paper, in order to cover $|k|$ up to $19.0\,\mathrm{cm}^{-1}$, cf. (16). As expected from the k-spectrum with $M = 5$ of the same simulation, shown (for slightly different synthetic PCI parameters) in figure 5 of [45], the k-spectrum follows a power law with an exponent close to -5 when $|k| > 3.6\,\mathrm{cm}^{-1}$, further substantiating the universal character of this exponent. The larger k-region covered for $M = 3$ does, however, show that a transition to a steeper power law, with an exponent near -10, occurs for $|k| > 11.9\,\mathrm{cm}^{-1}$, while the flattening at the largest $|k|$ is again attributed to aliasing. The exponent for $|k| > 11.9\,\mathrm{cm}^{-1}$ is significantly changed (from -9.8 ± 0.4 to -3.9 ± 0.5) by the inclusion of noise, which once again reduces the steepness of the k-spectrum at low psd. We note that the large-$|k|$ exponent in figure 10 is different from that of the AE simulation in figure 9, indicating that it is not universal, but that the transition occurs at similar psd values, making it plausible that the transition is related to numerical hyper-diffusion becoming dominant at low psd and high $|k|$.

3.1.4. Consistency of the PCI signal and line-integrated fluctuating electron density We lastly check whether the synthetic PCI k-spectra resemble those of $\int_{\mathrm{LoS}} \tilde{n}_e \,\mathrm{d}z$, for which they are used as a proxy. This is necessary if direct comparisons between PCI k-spectra and theoretical k-spectra of $\tilde{n}_e$ are to be meaningful. Figure 11 shows the k-spectra of $\int_{\mathrm{LoS}} \tilde{n}_e \,\mathrm{d}z$ (computed in the same way as those of the synthetic PCI signal for a line at $y = 0$) from the low-β KE and AE simulations in the upper and lower panes, respectively. In both cases, the k-spectra of $\int_{\mathrm{LoS}} \tilde{n}_e \,\mathrm{d}z$ follow distinct power laws in similar k-ranges to those of the PCI signal in figure 9, indicating that the PCI k-spectra correctly capture the transition points. We also note that the v_{ph}-values obtained from the PCI spectrum of the KE simulation are consistent with the v_{ph}-values obtained from $\int_{\mathrm{LoS}} \tilde{n}_e \,\mathrm{d}z$, as expected based on [25]. The exponents found in figure 11 are further almost identical to those in figure 9 at lower $|k|$-values. In the KE case, exponents close to -3, -6, and -4.5 are found for $|k| < 5.5\,\mathrm{cm}^{-1}$, $|k| \in [5.5\,\mathrm{cm}^{-1}, 10.6\,\mathrm{cm}^{-1}]$, and $|k| > 10.6\,\mathrm{cm}^{-1}$, respectively, in agreement with the exponents of figure 9. In the AE case, exponents close to -1 and -5 are recovered for $|k| < 10.1\,\mathrm{cm}^{-1}$, while the exponent for $|k| > 10.1\,\mathrm{cm}^{-1}$ is modified from -9.0 ± 0.4 to -6.5 ± 0.1. The faster decay of the synthetic PCI k-spectrum at high $|k|$-values compared with the k-spectrum of $\int_{\mathrm{LoS}} \tilde{n}_e \,\mathrm{d}z$ is caused by the integration over the detector elements. We note that the addition of noise also reduces the steepness of the k-spectra at high $|k|$ (low psd), but that it will not necessarily make the resulting k-spectra resemble those of $\int_{\mathrm{LoS}} \tilde{n}_e \,\mathrm{d}z$.

3.2. EUTERPE

We now briefly discuss the results obtained by applying the synthetic PCI diagnostic to a simulation performed with the EUTERPE code. EUTERPE is a global gyrokinetic particle-in-cell code for stellarator geometries, which has recently been extended to allow nonlinear simulations with AEs [51]. The run to which the synthetic diagnostic is applied

utilizes the W7-X standard configuration and is described in section 5 of [51]. Synthetic PCI results related to the run have already been presented in [45]. While the precise parameters used for the synthetic PCI diagnostic in [45] differ from those used in the present work, the figures in [45] are still useful for illustrative purposes; all numbers quoted below are, however, based on the parameters of the present work ($P_0 = 6.3\,\mathrm{W}$, $M = 5$, $W_0 = 4\,\mathrm{cm}$, and $a = 6.8\,\mathrm{cm}$). Additionally, [45] did not include quantitative estimates of v_{ph} or the uncertainties of the fitted exponents, which are given below. The basic parameters of the extracted $\tilde{n}_e$ profile are seen in table 1 and the background profiles are shown in figure 18 of [51]. As the investigations in [51] focused on the central part of the plasma, the simulation only includes $\psi < 0.45$.

3.2.1. Results The main difference between the (k, f)-spectra obtained from the EUTERPE simulation, illustrated in figure 3 of [45], and the GENE-3D simulations is the significantly smaller v_{ph} obtained from the EUTERPE simulation; using the method of [25], $v_{\mathrm{ph}} = 750\,\mathrm{m/s}$ and $-600\,\mathrm{m/s}$ are found from the full LoSs in the EUTERPE simulation, while the corresponding values from the low-β KE GENE-3D simulation were $4.9\,\mathrm{km/s}$ and $-5.7\,\mathrm{km/s}$. This is attributed to the different plasma parameters and radial range used in the EUTERPE simulation, compare figure 18 of [51] with figure 6. The k-spectrum in the EUTERPE simulation, illustrated in figure 4 of [45], follows a power law with an exponent of -1.3 ± 0.2 for $|k| < 5.7\,\mathrm{cm}^{-1}$ and an exponent of -4.7 ± 0.4 for $|k| > 5.7\,\mathrm{cm}^{-1}$; the addition of noise leads to a negligible change of the exponents. These values are close to the low-$|k|$ exponents of the GENE-3D low-β AE simulation from figure 9, and an exponent close to -5 also occurs in the AE simulation of the W7-X standard configuration from [49] in figure 10. Additionally, exponents close to -5 have been found in the k-spectra of experimental observations [58], other numerical simulations of ITG turbulence [61], and analytical theory [59, 60, 63], indicating their universal character for turbulence with an AE response. We finally note that a reduction of M in the EUTERPE simulation is not meaningful, since its θ^* step size is approximately four times larger than that of the GENE-3D simulations, resulting in the resolution of the PCI detector elements already being approximately equal to that of the simulation around $\psi = 0.45$ for $M = 5$.

3.3. Summary

To summarize the findings of this section, the rotation direction and v_{ph} may be determined based on the (k, f)-spectra of the synthetic PCI signal, in agreement with [25, 45]. Additionally, the synthetic PCI k-spectra resemble the k-spectra of $\int_{\mathrm{LoS}} \tilde{n}_e \,\mathrm{d}z$, although the decay rate at large $|k|$ is different in some cases due to the integration over the detector elements. The above investigations further show that the k-spectra are distinct for KE and AE simulations, and that the exponents obtained are in agreement with previous experimental [16, 58, 63], numerical [61], and analytical [59, 60, 62, 63] predictions. We particularly note that a k-range with a psd $\propto |k|^{-5}$ has been observed

in all AE simulations investigated, indicating the existence of universal $\tilde{n}_e$ turbulence features in the spectral range of the PCI diagnostic at W7-X. The fact that the exponents are explainable based on models that do not explicitly include curvature of the magnetic field, e.g., [60, 62], may further indicate that the basic features of fully developed turbulence in W7-X can be investigated using a slab-like framework. This is consistent with stellarator turbulence being more slab-like than tokamak turbulence [1].

4. Conclusion and outlook

In this paper, the development of a synthetic PCI diagnostic for turbulence studies at W7-X, consisting of an instrument response model and gyrokinetic models of the fluctuating electron density observed by the PCI system, has been described. The instrument response model is based on [17, 28]. It includes diffraction from an aperture before the detectors, the cutoff at low wave numbers caused by the PCI phase plate, integration of the beam power over the detector elements, the effects of magnification, and detector noise. The instrument response model was verified by application to a model sound wave calibration signal from [24, 54], which also enabled the calculation of a synthetic calibration factor. Synthetic PCI signals were then obtained from fluctuating electron density profiles computed using the global, nonlinear gyrokinetic codes GENE-3D [47–50] and EUTERPE [51]. The GENE-3D investigations were based on results from three simulations of the W7-X standard configuration, one of which included a kinetic electron response, while the remaining two utilized adiabatic electrons. The plasma rotation direction and PCI phase velocity in the simulations could be determined based on wave number-frequency spectra, validating experimental expectations [25]. Further, the investigations showed that, in the absense of a neoclassical radial electric field, the rotation direction was determined by zonal flows, which could reverse and did not necessarily have any relation to the rotation direction of the underlying linear modes. We also investigated the wave number spectra obtained from the GENE-3D simulations by the synthetic PCI diagnostic, which allowed differences between the kinetic and adiabatic electron runs to be established, as well as comparison with theoretical and experimental results. The adiabatic electron wave number spectra were found to follow a power law with an exponent close to -5 for sufficiently large wave numbers, in agreement with theoretical models [59, 60, 63], previous gyrokinetic simulations of pure ITG turbulence [61], and experimental results from an early stellarator experiment [58]. The kinetic electron simulation was found to follow steeper power laws than the adiabatic electron simulations, in agreement with the theoretical model of [62] and experimental results from the Tore Supra tokamak [16]. These results indicate that the PCI system may be able to investigate universal features of the electron density fluctuations associated with turbulence at W7-X. We further note that the wave number spectra could be explained by models ignoring magnetic field curvature [60, 62], indicating that the basic features of saturated turbulence in W7-X may be investigated using a slab-like framework. The EUTERPE simulation, which was described in [51], utilized

adiabatic electrons and generally yielded similar results to the GENE-3D simulations with adiabatic electrons; further details of the synthetic PCI diagnostic investigations of the EUTERPE simulation are found in [45].

Several points of interest remain for future synthetic PCI diagnostic development and investigations at W7-X. First, it will be interesting to utilize the synthetic PCI diagnostic for general interpretation and planning of experiments in the upcoming long-pulse campaigns at W7-X. Second, current efforts to include a radial localization mask model [24,29,30] in the synthetic PCI diagnostic will be useful for interpreting the results of experiments utilizing such masks in previous and future W7-X operation phases [24]. Third, it is of interest to analyze other global, nonlinear gyrokinetic simulations of W7-X as they become available, in order to facilitate the investigation of stellarator turbulence. This goal may be achieved through the integration of other gyrokinetic codes, e.g., GTC [52, 53] and XGC-S [66], with the synthetic PCI diagnostic, as well as through future GENE-3D and EUTERPE runs. For example, global, nonlinear gyrokinetic simulations including a neoclassical radial electric field, which is the main parameter determining the experimentally observed PCI phase velocity [25], have only been performed with GTC (utilizing adiabatic electrons) at present [53], making the ongoing effort to integrate GTC in the synthetic PCI diagnostic interesting; we do, however, note that linear EUTERPE simulations with a neoclassical radial electric field have been performed [67, 68] and that efforts to include a neoclassical radial electric field in GENE-3D are ongoing as well. Future simulations of interest for synthetic PCI investigations will include kinetic electron simulations with a neoclassical radial electric field and realistic plasma parameters, as these are the minimum requirements to produce electron density fluctuations resembling the ones observed by the actual PCI system at W7-X. It will be useful to perform such simulations both of standard ECRH plasmas and high-performance plasmas, e.g., found during pellet [7] or neutral beam [10] injection. Fourth, the inclusion of magnetohydrodynamic models in the synthetic PCI diagnostic, as done in [34–37], could facilitate the investigation of such activity with PCI at W7-X. Fifth, to utilize the planned acousto-optical modulator upgrade of the PCI system for the investigation of mode conversion of waves from the W7-X ion cyclotron resonance heating system, which will start operating in the next experimental campaign [69], the integration of full-wave codes with the synthetic PCI diagnostic, as done by [29, 32, 38], will be of interest. Finally, the inclusion of a synthetic interferometry diagnostic will be useful if the PCI system is augmented by an interferometer to enable the study of long-wavelength modes, as done on DIII-D [22, 23].

Acknowledgments

SKH acknowledges support by an Internationalisation Fellowship (CF19-0738) from the Carlsberg Foundation. Support for the MIT and SUNY-Cortland participation was provided by the US Department of Energy, Grant DE-SC0014229. This work has been carried out within the framework of the EUROfusion Consortium, funded by the

European Union via the Euratom Research and Training Programme (Grant Agreement No 101052200 — EUROfusion). Views and opinions expressed are however those of the author(s) only and do not necessarily reflect those of the European Union or the European Commission. Neither the European Union nor the European Commission can be held responsible for them.

Appendix A. Sound wave calibration

We compute the equivalent line-integrated electron density along the PCI LoSs for sound wave calibration, $(\int_{\mathrm{LoS}} \tilde{n}_e \,\mathrm{d}z)_{\mathrm{cal}}$, given in (24). To do this, we first assume the air around the speaker to have constant molecular polarizability and a refractive index, N_{cal}, close to 1. The Lorentz−Lorenz equation [55] then yields the following linear relation between N_{cal} and the density of the air around the speaker, ϱ_{cal},

$$N_{\mathrm{cal}} \approx 1 + (N_0 - 1)\frac{\varrho_{\mathrm{cal}}}{\varrho_0}, \tag{A.1}$$

where $\varrho_0 = 1.2256\,\mathrm{kg/m^3}$ is the reference density at which $N_{\mathrm{cal}} = N_0$; for the standard atmosphere, $N_0 - 1 = 2.726 \times 10^{-4}$ [31]. The sound wave introduces a density fluctuation, $\tilde{\varrho}$, around ϱ_0, such that $\varrho_{\mathrm{cal}} = \varrho_0 + \tilde{\varrho}$, yielding

$$N_{\mathrm{cal}} \approx N_0 + (N_0 - 1)\frac{\tilde{\varrho}}{\varrho_0}. \tag{A.2}$$

From (A.2), it is clear that the fluctuating refractive index associated with the sound wave, $\tilde{N}_{\mathrm{cal}}$, may be expressed as $\tilde{N}_{\mathrm{cal}} = (N_0 - 1)\tilde{\varrho}/\varrho_0$, giving the fluctuating phase shift

$$\tilde{\phi}_{\mathrm{cal}} = \frac{2\pi}{\lambda_0}\int_{\mathrm{LoS}} \tilde{N}_{\mathrm{cal}}\,\mathrm{d}z = \frac{2\pi(N_0 - 1)}{\lambda_0 \varrho_0}\int_{\mathrm{LoS}} \tilde{\varrho}\,\mathrm{d}z. \tag{A.3}$$

We can further rewrite (A.3) in terms of the pressure fluctuation, $\tilde{p}$, around the reference pressure, $p_0 = 101.325\,\mathrm{kPa}$, by noting that the response to the sound wave can be assumed to be adiabatic, meaning that $\tilde{\varrho} = \varrho_0 \tilde{p}/(\gamma p_0)$, where $\gamma = 1.4$ is the adiabatic index of dry air at 293 K. With this,

$$\tilde{\phi}_{\mathrm{cal}} = \frac{2\pi(N_0 - 1)}{\lambda_0 \gamma p_0}\int_{\mathrm{LoS}} \tilde{p}\,\mathrm{d}z. \tag{A.4}$$

Remembering that $\tilde{\phi} = -r_e \lambda_0 \int_{\mathrm{LoS}} \tilde{n}_e \,\mathrm{d}z$ in the presence of the plasma finally allows us to compute $(\int_{\mathrm{LoS}} \tilde{n}_e \,\mathrm{d}z)_{\mathrm{cal}}$,

$$\left(\int_{\mathrm{LoS}} \tilde{n}_e \,\mathrm{d}z\right)_{\mathrm{cal}} = -\frac{2\pi(N_0 - 1)}{r_e \lambda_0^2 \gamma p_0}\int_{\mathrm{LoS}} \tilde{p}\,\mathrm{d}z, \tag{A.5}$$

which is the expression from (24) that has the same absolute value as the expression from [31], but opposite sign.

A simple calibration factor, F_{cal}, may be obtained by dividing the average $(\int_{\mathrm{LoS}} \tilde{n}_e \,\mathrm{d}z)_{\mathrm{cal}}$ over a detector element by the corresponding $\tilde{S}_{\mathrm{cal}}$. Since use of the instantaneous values may lead to numerical problems at points where the signals approach zero, the ratio can instead be taken between peak or temporal root mean square values, with the appropriate sign change to account for the opposite signs

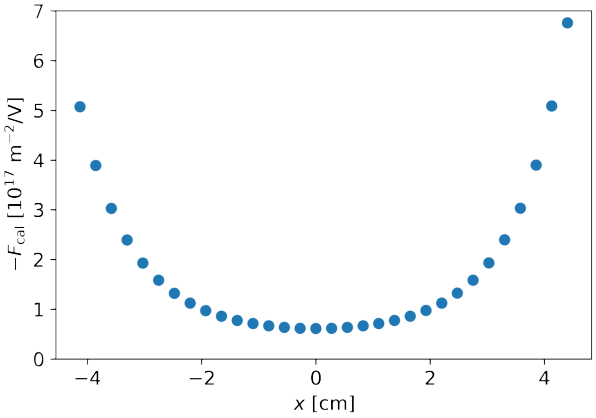

Figure A1. (Negative) calibration factor obtained for each detector element from the calibration signal of figure 3.

of $(\int_{\mathrm{LoS}} \tilde{n}_e \,\mathrm{d}z)_{\mathrm{cal}}$ and $\tilde{S}_{\mathrm{cal}}$. The relative difference between the peak and root mean square calibration factors is $< 10^{-3}$ for the numerical scheme used in this work, but since the root mean square value matches the experimental calibration method more closely [24, 54], it is preferred over the peak value. Thus, we arrive at

$$F_{\mathrm{cal}} = -\frac{1}{M^2 A_{\mathrm{det}} \tilde{S}_{\mathrm{cal}}^{\mathrm{rms}}} \left\{ \left[\int_{M\times\mathrm{det}} \left(\int_{\mathrm{LoS}} \tilde{n}_e \,\mathrm{d}z \right)_{\mathrm{cal}} \right] \mathrm{d}\mathbf{x}_\perp \right\}^{\mathrm{rms}} . \tag{A.6}$$

The calibrated signal $F_{\mathrm{cal}}\tilde{S}$ corresponds to the actual $\int_{\mathrm{LoS}} \tilde{n}_e \,\mathrm{d}z$ averaged over the image of the detector elements for Fourier components with $|k_x| > k_{\mathrm{min}}$, but still includes the suppression of components with $|k_x| \leq k_{\mathrm{min}}$; noise may be included by replacing $\tilde{S}$ with S. As a final point, we plot $-F_{\mathrm{cal}}$ obtained from the calibration signal of figure 3 in figure A1. As expected from (A.6), $-F_{\mathrm{cal}}$ in figure A1 increases when the amplitude of $\tilde{S}_{\mathrm{cal}}$ decreases, cf. figure 3.

References

[1] Helander P, Beidler C D, Bird T M, Drevlak M, Feng Y, Hatzky R, Jenko F, Kleiber R, Proll J H E, Turkin Y and Xanthopoulos P 2012 *Plasma Phys. Control. Fusion* **54** 124009

[2] Beidler C D, Smith H M, Alonso A, Andreeva T, Baldzuhn J, Beurskens M N A, Borchardt M, Bozhenkov S A, Brunner K J, Damm H, Drevlak M, Ford O P, Fuchert G, Geiger J, Helander P, Hergenhahn U, Hirsch M, Höfel U, Kazakov Y O, Kleiber R, Krychowiak M, Kwak S, Langenberg A, Laqua H P, Neuner U, Pablant N A, Pasch E, Pavone A, Pedersen T S, Rahbarnia K, Schilling J, Scott E R, Stange T, Svensson J, Thomsen H, Turkin Y, Warmer F, Wolf R C, Zhang D and the W7-X Team 2021 *Nature* **596** 221–226

[3] Klinger T *et al* 2019 *Nucl. Fusion* **59** 112004

[4] Plunk G G, Xanthopoulos P, Weir G M, Bozhenkov S A, Dinklage A, Fuchert G, Geiger J, Hirsch M, Hoefel U, Jakubowski M, Langenberg A, Pablant N, Pasch E, Stange T, Zhang D and the W7-X Team 2019 *Phys. Rev. Lett.* **122** 035002

[5] Proll J H E, Helander P, Connor J W and Plunk G G 2012 *Phys. Rev. Lett.* **108** 245002

[6] Alcusón J A, Xanthopoulos P, Plunk G G, Helander P, Wilms F, Turkin Y, von Stechow A and Grulke O 2020 *Plasma Phys. Control. Fusion* **62** 035005

[7] Xanthopoulos P, Bozhenkov S A, Beurskens M N, Smith H M, Plunk G G, Helander P, Beidler C D, Alcusón J A, Alonso A, Dinklage A, Ford O, Fuchert G, Geiger J, Proll J H E, Pueschel M J, Turkin Y, Warmer F and the W7-X Team 2020 *Phys. Rev. Lett.* **125** 075001
[8] Nespoli F, Masuzaki S, Tanaka K, Ashikawa N, Shoji M, Gilson E P, Lunsford R, Oishi T, Ida K, Yoshinuma M, Takemura Y, Kinoshita T, Motojima G, Kenmochi N, Kawamura G, Suzuki C, Nagy A, Bortolon A, Pablant N A, Mollen A, Tamura N, Gates D A and Morisaki T 2022 *Nat. Phys.* **18** 350–356
[9] Di Siena A, Bañón Navarro A and Jenko F 2020 *Phys. Rev. Lett.* **125** 105002
[10] Huang Z, Edlund E, Porkolab M, von Stechow A, Bähner J-P, Hansen S K, Grulke O, Ford O P, Beurskens M N A, Bozhenkov S A, Lazerson S and the Wendelstein 7-X Team 2021 *Europhys. Conf. Abstracts* **45A** P2.1062 URL `http://ocs.ciemat.es/EPS2021PAP/pdf/P2.1062.pdf`
[11] Liu S C, Liang Y, Wang H Q, Killer C, Drews P, Knieps A, Han X, Grulke O, Krämer-Flecken A, Xu G S, Yan N, Höschen D, Nicolai D, Satheeswaran G, Geiger J, Henkel M, Huang Z, König R, Li Y, Neubauer O, Rahbarnia K, Sandri N, Schweer B, Wang E H, Wang Y M, Xu S, Gao X and W7-X Team 2020 *Phys. Plasmas* **27** 122504
[12] Pinzón J R, Happel T, Blanco E, Conway G D, Estrada T and Stroth U 2017 *Plasma Phys. Control. Fusion* **59** 035005
[13] Happel T, Görler T, Hennequin P, Lechte C, Bernert M, Conway G D, Freethy S J, Honoré C, Pinzón J R, Stroth U and The ASDEX Upgrade Team 2017 *Plasma Phys. Control. Fusion* **59** 054009
[14] Lechte C, Conway G D, Görler T, Tröster-Schmid C and the ASDEX Upgrade Team 2017 *Plasma Phys. Control. Fusion* **59** 075006
[15] Estrada T, Carralero D, Windisch T, Sánchez E, García-Regaña J M, Martínez-Fernández J, de la Peña A, Velasco J L, Alonso J A, Beurskens M, Bozhenkov S, Damm H, Fuchert G, Kleiber R, Pablant N, Pasch E and the W7-X team 2021 *Nucl. Fusion* **61** 046008
[16] Hennequin P, Sabot R, Honoré C, Hoang G T, Garbet X, Truc A, Fenzi C and Quéméneur A 2004 *Plasma Phys. Control. Fusion* **46** B121–133
[17] Weisen H 1988 *Rev. Sci. Instrum.* **59** 1544–1549
[18] Coda S, Porkolab M and Carlstrom T N 1992 *Rev. Sci. Instrum.* **63** 4974–4976
[19] Marinoni A, Coda S, Chavan R and Pochon G 2006 *Rev. Sci. Instrum.* **77** 10E929
[20] Rost J C, Lin L and Porkolab M 2010 *Phys. Plasmas* **17** 062506
[21] Edlund E M, Porkolab M, Huang Z, Grulke O, Böttger L-G, von Sehren C and von Stechow A 2018 *Rev. Sci. Instrum.* **89** 10E105
[22] Davis E M, Rost J C, Porkolab M, Marinoni A and Van Zeeland M A 2018 *Rev. Sci. Instrum.* **89** 10B106
[23] Rost J C, Davis E M, Marinoni A, Porkolab M and Van Zeeland M A 2019 *J. Instrum.* **14** C12023
[24] Huang Z, Edlund E, Porkolab M, Bähner J-P, Böttger L-G, von Sehren C, von Stechow A and Grulke O 2021 *J. Instrum.* **16** P01014
[25] Bähner J-P, Alcusón J A, Hansen S K, v Stechow A, Grulke O, Windisch T, Smith H M, Huang Z, Edlund E, Porkolab M, Beurskens M N A, Bozhenkov S A, Ford O P, Pablant N, Plunk G G, Bañón Navarro A, Jenko F and The W7-X Team 2021 *J. Plasma Phys.* **87** 905870314
[26] Zernike F 1934 *Physica* **1** 689–704
[27] Presby H M and Finkelstein D 1967 *Rev. Sci. Instrum.* **38** 1563–1572
[28] Coda S 1997 *An Experimental Study of Turbulence by Phase-Contrast Imaging in the DIII-D Tokamak* Ph.D. thesis Massachusetts Institute of Technology Cambridge URL `https://dspace.mit.edu/handle/1721.1/10748`
[29] Porkolab M, Rost J C, Basse N, Dorris J, Edlund E, Lin L, Lin Y and Wukitch S 2006 *IEEE Trans. Plasma Sci.* **34** 229–234
[30] Dorris J R, Rost J C and Porkolab M 2009 *Rev. Sci. Instrum.* **80** 023503
[31] Mazurenko A 2001 *Phase Contrast Imaging on the Alcator C-Mod Tokamak* Ph.D. thesis Massachusetts Institute of Technology Cambridge URL `https://dspace.mit.edu/handle/`

1721.1/93210

[32] Nelson-Melby E, Porkolab M, Bonoli P T, Lin Y, Mazurenko A and Wukitch S J 2003 *Phys. Rev. Lett.* **90** 155004

[33] Lin L, Porkolab M, Edlund E M, Rost J C, Fiore C L, Greenwald M, Lin Y, Mikkelsen D R, Tsujii N and Wukitch S J 2009 *Phys. Plasmas* **16** 012502

[34] Edlund E M 2009 *A Study of Reversed Shear Alfvén Eigenmodes in Alcator C-Mod with Phase Contrast Imaging* Ph.D. thesis Massachusetts Institute of Technology Cambridge URL https://dspace.mit.edu/handle/1721.1/63004

[35] Edlund E M, Porkolab M, Kramer G J, Lin L, Lin Y and Wukitch S J 2009 *Phys. Rev. Lett.* **102** 165003

[36] Edlund E M, Porkolab M, Kramer G J, Lin L, Lin Y and Wukitch S J 2009 *Phys. Plasmas* **16** 056106

[37] Edlund E M, Porkolab M, Kramer G J, Lin L, Lin Y, Tsujii N and Wukitch S J 2010 *Plasma Phys. Control. Fusion* **52** 115003

[38] Tsujii N, Porkolab M, Bonoli P T, Edlund E M, Ennever P C, Lin Y, Wright J C, Wukitch S J, Jaeger E F, Green D L and Harvey R W 2015 *Phys. Plasmas* **22** 082502

[39] Huang Z 2017 *Experimental study of plasma turbulence in the TCV tokamak* Ph.D. thesis École Polytechnique Fédérale de Lausanne Lausanne URL https://infoscience.epfl.ch/record/230348

[40] Iantchenko A, Merlo G, Carpanese F, Vallar M, Brunner S and Coda S 2021 *Europhys. Conf. Abstracts* **45A** P4.1064 URL http://ocs.ciemat.es/EPS2021ABS/pdf/P4.1064.pdf

[41] Gong S B, Yu Y, Xu M, Jiang W, Zhong W L, Shi Z B, Wang H J, Wu Y F, Yuan B D, Lan T, Ye M Y, Duan X R and HL-2A team 2017 *Fusion Eng. Des.* **123** 802–806

[42] Tanaka K, Vyacheslavov L N, Akiyama T, Sanin A, Kawahata K, Tokuzawa T, Ito Y, Tsuji-Iio S and Okajma S 2003 *Rev. Sci. Instrum.* **74** 1633–1637

[43] Tanaka K, Michael C A, Vyacheslavov L N, Sanin A L, Kawahata K, Akiyama T, Tokuzawa T and Okajima S 2008 *Rev. Sci. Instrum.* **79** 10E702

[44] Böttger L-G 2019 *Phase Contrast Imaging: A Turbulence Diagnostic for the Wendelstein 7-X Stellarator* Ph.D. thesis Technical University of Denmark Kgs. Lyngby URL https://backend.orbit.dtu.dk/ws/portalfiles/portal/195823265/Lukas_Georg_B_ttger.pdf

[45] Hansen S K, Porkolab M, Huang Z, Bähner J-P, von Stechow A, Grulke O, Edlund E M, Bañón Navarro A, Sánchez E and the Wendelstein 7-X Team 2021 *Europhys. Conf. Abstracts* **45A** P3.1078 URL http://ocs.ciemat.es/EPS2021PAP/pdf/P3.1078.pdf

[46] Terry P W, Greenwald M, Leboeuf J-N, McKee G R, Mikkelsen D R, Nevins W M, Newman D E, Stotler D P, Task Group on Verification and Validation, US Burning Plasma Organization and US Transport Task Force 2008 *Phys. Plasmas* **15** 062503

[47] Maurer M 2020 *GENE-3D - a global gyrokinetic turbulence code for stellarators and perturbed tokamaks* Ph.D. thesis Technische Universität München Garching URL https://mediatum.ub.tum.de/doc/1539628/1539628.pdf

[48] Maurer M, Bañón Navarro A, Dannert T, Restelli M, Hindenlang F, Görler T, Told D, Jarema D, Merlo G and Jenko F 2020 *J. Comput. Phys.* **420** 109694

[49] Bañón Navarro A, Merlo G, Plunk G G, Xanthopoulos P, von Stechow A, Di Siena A, Maurer M, Hindenlang F, Wilms F and Jenko F 2020 *Plasma Phys. Control. Fusion* **62** 105005

[50] Wilms F, Bañón Navarro A, Merlo G, Leppin L, Görler T, Dannert T, Hindenlang F and Jenko F 2021 *J. Plasma Phys.* **87** 905870604

[51] Sánchez E, Mishchenko A, García-Regaña J M, Kleiber R, Bottino A, Villard L and the W7-X team 2020 *J. Plasma Phys.* **86** 855860501

[52] Wang H Y, Holod I, Lin Z, Bao J, Fu J Y, Liu P F, Nicolau J H, Spong D and Xiao Y 2020 *Phys. Plasmas* **27** 082305

[53] Fu J Y, Nicolau J H, Liu P F, Wei X S, Xiao Y and Lin Z 2021 *Phys. Plasmas* **28** 062309

[54] Bähner J-P, von Stechow A, Huang Z, Edlund E, Porkolab M and Grulke O 2020 PCI soundwave

calibration for relative fluctuation amplitude comparison URL `https://wikis.ipp-hgw.mpg.de/E5_diagnostics/images/9/95/PCI_Calibration_jpb.pdf`

[55] Born M and Wolf E 2002 *Principles of Optics* 7th (expanded) ed (Cambridge: Cambridge University Press)

[56] Swanson D G 2003 *Plasma Waves* 2nd ed (Bristol: IOP Publishing)

[57] van Vilet K M 1967 *Appl. Opt.* **6** 1145–1168

[58] Bol K 1964 *Phys. Fluids* **7** 1855–1862

[59] Chen F F 1965 *Phys. Rev. Lett.* **15** 381–383

[60] Tchen C M, Pécseli H L and Larsen S E 1980 *Plasma Phys.* **22** 817–829

[61] Görler T and Jenko F 2008 *Phys. Plasmas* **15** 102508

[62] Gürcan Ö D, Garbet X, Hennequin P, Diamond P H, Casati A and Falchetto G L 2009 *Phys. Rev. Lett.* **102** 255002

[63] Pécseli H L 2015 *Ann. Geophys.* **33** 875–900

[64] Grimm R C, Greene J M and Johnson J L 1976 Computation of the magnetohydrodynamic spectrum in axisymmetric toroidal confinement systems *Controlled Fusion* (*Methods in Computational Physics: Advances in Research and Applications* vol 16) ed Killeen J (Amsterdam: Elsevier) pp 253–280

[65] Hirshman S P, van Rij W I and Merkel P 1986 *Comput. Phys. Commun.* **43** 143–155

[66] Cole M D J, Moritaka T, Hager R, Dominski J, Ku S and Chang C S 2020 *Phys. Plasmas* **27** 044501

[67] Riemann J, Kleiber R and Borchardt M 2016 *Plasma Phys. Control. Fusion* **58** 074001

[68] Sánchez E, Estrada T, Velasco J L, Calvo I, Cappa A, Alonso A, García-Regaña J M, Kleiber R, Riemann J and the TJ-II Team 2019 *Nucl. Fusion* **59** 076029

[69] Schweer B, Ongena J, Borsuk V, Birus D, Bozhenkov S, Castaño Bardawil D, Durodié F, Hartmann D, Hollfeld K P, Kallmeyer P, Krivska A, Louche F, Messiaen A, Neubauer O, Offermanns G, Satheeswaran G, Van Schoor M, Vervier M, Wolf R and the W7-X team 2017 *Fusion Eng. Des.* **123** 303–308